UiO : Department of Geosciences
University of Oslo

# Filtering sources of false alarms from automatically detected avalanches in Sentinel-1 SAR images

**Maria Flaten**

Master's Thesis, Spring 2023

Title: Filtering sources of false alarms from automatically detected avalanches in Sentinel-1 SAR images

Supervisor: Karsten Müller [1,2]
Co-supervisor: Markus Eckerstorfer [2]

1: University of Oslo
2: The Norwegian Water Resources and Energy Directorate (NVE)

Data associated with this work have been made available on GitHub
https://github.com/NVE/satskred/tree/master/greenness

This work is published digitally through DUO – Digitale Utgivelser ved UiO
http://www.duo.uio.no/

Printed: Graphic Centre, University of Oslo

# Abstract

This study analyses automatically detected avalanche deposits in Sentinel-1 SAR images by the SatSkred algorithm from the three winter seasons 2018/19, 2019/20 and 2020/21. SatSkred allows for near-real-time automatic avalanche detection, but previous studies indicate great over-detection due to misinterpreted signatures in the change detection images. By inspecting scenarios in the dataset with high avalanche activity, we aim to discern patterns for false positive detections and suggest concepts for improvement, which the developers can use to increase the true detection accuracy. We have inspected smaller areas in a total of 16 RGB-change detection images. By developing a Greenness Indicator, we have quantified the band values in RGB-composites to explain the relative change in backscatter. Further, this was used to analyse the greenness in non-avalanche terrain, avalanche terrain, detection area, and a 40 meters buffer zone in potentially true and false change detection scenarios. The greenness in non-avalanche terrain correlated highly with the avalanche terrain (corr = 0.85), while the greenness in the detection area correlated highly with the buffer zone (corr = 0.74). We found no dependence between the avalanche terrain and the detection area. Our results indicate that a contrast of minimum 0.25 between the buffer zone and detection area excluded 83% of the potentially false detections while including 92% of the potentially true detections. Following, a contrast of minimum 0.48 between the avalanche terrain and the detected area excluded 78% of the potentially false detections and included 73% of the potentially true detections. The thresholds were further tested in two case studies with changing meteorological conditions. Our case studies revealed high sensitivity to the threshold of 0.48 between the avalanche terrain and the detected area, indicating a high potential for false positive errors. Our findings indicate a potential for false detections to be filtered by the proposed threshold value between the detections and the surrounding buffer areas.

# Acknowledgements

As I now deliver my master's thesis, I can look back on five wonderful years at Blindern. First and foremost, I would like to thank my supervisors, Karsten Müller and Markus Eckerstorfer. Thank you for your trust, and for giving me the opportunity to work with you on the SatSkred project. Karsten, you are a fantastic professor, and it has been fun to learn from your field of expertise. Max, it has been an honour to work with you and get to know you. Your support and feedback are greatly appreciated and have helped me challenge and develop myself.

I also want to take this opportunity to thank friends and co-students at Blindern. A big thank you also goes to former colleagues and friends in GÆA Norvegica, for all the social and fun activities we have engaged in over the past few years. A special thanks go to Camilla and Sissel for proofreading my work and for helping me improve my language. Thanks to family and friends back home. Mom and dad, thank you for all the love and encouragement. And last but not least, Henrik. Thank you so much for everything you have contributed here at home to make this work, and for doing your best every day to cheer me up. It means everything to me.

# Contents

# CHAPTER 1

# Introduction

## 1.1 Background

Snow avalanches (hereafter avalanches) have caused 104 fatalities in Norway since the winter season of 2008/09 (Varsom, 2023). Increased interest in backcountry use in the winter increases the vulnerability to avalanche hazards in mountainous regions. Avalanche forecasting is one of the most important mitigation measures against severe avalanche accidents (McClung, 2002). The primary sources of a precise avalanche forecast are snowpack assessments put in context with meteorological data. It is also necessary to combine triggering factors with direct avalanche observations to avoid biases in forecasting (McClung, 2002). Nevertheless, accurate avalanche observations consistent in space and time are difficult to come by with traditional field-based methods, especially in regional-wide monitoring.

The European satellites Sentinel-1 A and B have operated since 2014 and 2016, respectively, orbiting near-polar ascending towards and descending from the North Pole (Sentinel 1B out of order since 2022). The active radar sensor onboard the satellites captures radar images all over the planet with a repeat cycle of minimum 6 days. The recent development of an automatic processing chain allows for the detection of avalanche debris in the SAR-images, resulting in near-real-time automatic avalanche detection (Eckerstorfer et al., 2019). By utilising a temporal change detection method, avalanche debris are detectable due to the relative increase in backscatter, originating from the increased backscatter coefficient of rougher, disturbed snow.

A consortium around the Norwegian Avalanche Warning Service (NAWS) operates continuous monitoring of avalanche activity over large parts of Norway using the SatSkred technology, with the intention to feed detected avalanches into the national avalanche database with information on size, timing, and location in the terrain. SatSkred has processed SAR images for avalanche-prone regions in Norway from November 2018 to May 2021. During this period, 243.000 avalanches have been detected by the automatic avalanche detection

algorithm. The number of detected avalanches varies from ∼18.500 in the season of 20/21 to ∼174.000 in the season of 19/20.

Variations in detected avalanche activity could be caused by varying snow conditions, constraints in detectability (e.g., differences in frequency of mapping in some areas), or other circumstances, such as other features on Earth's surface that resemble avalanches. It is known that various natural and artificial processes can cause signatures in the SAR data to be misinterpreted as debris. This can include ice-covered rivers and glacier melt, but also snow ploughing in urban or rural areas. While most of these so-called false alarms can be handled by the current system setup, some conditions leading to false detections still need to be identified and handled. Eckerstorfer et al., (2019) presented an average false alarm rate of 45.9% where the main source of falsely detected debris was the transition from wet to dry snow conditions. This transition is known to produce a relative increase in backscatter due to different dielectric properties in wet and dry snow (Eckerstorfer and Malnes, 2015).

## 1.2 Motivation and aim

Avalanche activity is a good indicator of avalanche danger. SatSkred provides a unique opportunity for near-real-time automatic avalanche detection and can be used to evaluate the accuracy of avalanche forecasts. A better understanding of when and where avalanches occur is gained by consistently monitoring avalanche-prone areas. It is more time efficient, and the algorithm remotely monitors all areas. This provides valuable information when mitigating loss of life and damaged infrastructure. However, the algorithm needs improvement to handle false detections. We aim that the detection accuracy will be improved by discerning a pattern for false detections and suggesting concepts to prevent these. The developers can then use our findings to improve the automatic detection system.

## 1.3 Objectives, research questions and hypothesis

In the RGB-composites used for avalanche detection, a relative increase in backscatter, in the case of an avalanche, is visible in green. The main reason for over-detecting in Sentinel-1 SAR images is the transition from wet to dry snow, leading to an overall increase in backscatter. Still, the phenomenon is unrelated to increased avalanche activity as the snowpack stabilises. The main objective of this study is to analyse if a greenness indicator can assist in finding false positives. A greenness indicator is introduced to monitor the relative change in backscatter by quantifying the band values in a RGB-change detection image. The greenness indicator is anticipated to explain the specific backscatter change in a pixel between the acquisition dates. We hypothesise that RGB-composites containing detections would exhibit an increased mean

greenness from the non-avalanche terrain to the avalanche terrain due to this is where avalanche debris is detected. Following, the mean greenness is expected to increase further from the avalanche terrain to the detection area, given a higher concentration of greenness. Furthermore, we anticipate a higher greenness in the detection area relative to the surrounding areas of undisturbed snow. Both RGB-composites with false and true detections are hypothesised to contain elevated greenness values between the zones; otherwise, no detections would have been identified.

We will conduct a zonal greenness analysis on scenarios in the dataset with high avalanche activity. We aim to answer the following research questions:

- By our greenness indicator, can we distinguish between the zones, as our hypothesis indicates?
- Can we separate between true and false detections based on mean greenness in zones or the contrast between zones?
- And if so, can we use our results to declare the detections in an unseen RGB-change detection image as true or false?

# CHAPTER 2

# Theoretical background

## 2.1 Avalanche types

A snow avalanche (hereafter avalanche) is a rapid downhill movement of snow debris, ice and rocks on a slope. Avalanches are classified according to their failure type, liquid water content or size. The two main failure types of avalanches are loose-snow and slab avalanches, seen in Figure 2.1 (McClung and Schaerer, 2006).

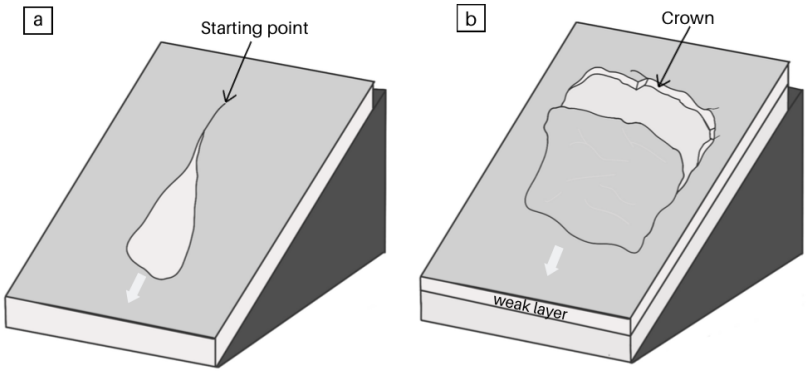


Figure 2.1: Illustration of a) loose-snow avalanche and b) slab avalanche failure mechanisms. a) Failure occurs in a single starting point, and results in a triangular shape when entraining snow downhill the slope. b) Failure occurs in a weak layer, resulting in the release of a cohesive slab. The crown indicates the starting point. Modified graphic from McClung and Schaerer (2006).

A loose-snow avalanche occurs in a relatively cohesionless surface layer (Figure 2.1a). A single point or area of new, dry or wet snow breaks away from the surrounding snow and starts sliding. The downhill movement forms a triangular shape. Snow accumulates into the flow as the sides spread, constantly increasing the mass. Loose-snow avalanches releases when the slope is steep enough to

overcome the cohesion and friction between the snow crystals (McClung and Schaerer, 2006).

A slab avalanche occurs when a cohesive layer of snow releases due to a failure in an underlying, weak layer (Figure 2.1b). The slab releases when the weak layer is unable to support its weight, i.e., if the gravitational force working on the slab is large enough to overcome the friction at the bed surface (Schweizer et al., 2015). The result is a block of snow entirely cut out by propagating fractures in the snow. Slab avalanches can be triggered by a person or an external force, e.g., a snowmobile or skier, gradual loading from precipitation, or changed snowpack properties due to surface warming (McClung and Schaerer, 2006).

### 2.1.1 Liquid water content

Avalanches are also classified by the presence or absence of liquid water content (LWC) in the snow, i.e., a wet or dry avalanches. The LWC is defined as the amount of water in the liquid phase within the snow, originating from either melt or rain (Fierz et al., 2009). The snow is classified from dry to soaked, depending on the range of LWC (Table 2.1). The presence of LWC and a (large) part of the snowpack being isothermal are prerequisites for the formation of wet-snow avalanches (Schweizer et al., 2015).

Table 2.1: Definition of snow based on liquid water content. The LWC range refers to volume fraction (Fierz et al., 2009).

| Term | Wetness index | LWC range [%] |
|---|---|---|
| Dry | 1 | 0 |
| Moist | 2 | 0-3 |
| Wet | 3 | 3-8 |
| Very wet | 4 | 8-15 |
| Soaked | 5 | >15 |

## 2.2 Avalanche path

An avalanche path indicates an area where avalanches occur (McClung and Schaerer, 2006). The path can be divided into three parts; the starting zone, the track and the runout zone shown in Figure 2.2.

The starting zone, or the release area, is where the initial failure in the snowpack occurs, and the snow begins to move. The upper limit of a starting zone is defined by the initiation point of a loose-snow avalanche or the crown of a slab avalanche (Figure 2.1). The track is where the snow is transported and accumulates mass as it moves downhill. This zone differs in majority depending on the size of the avalanche. The track is a significant terrain feature for large avalanches. For smaller avalanches, the track can be challenging to define. The

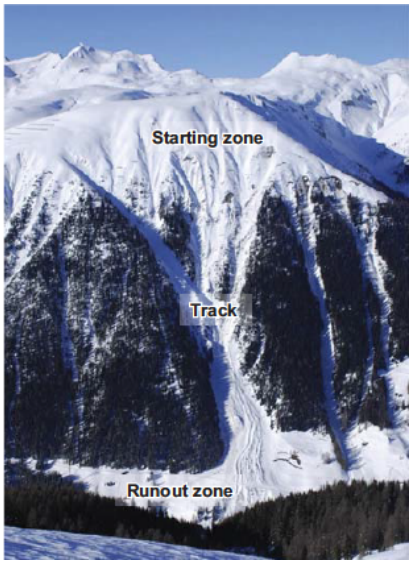


Figure 2.2: Illustration of an avalanche path, indicating the starting zone, track and runout zone. The figure is obtained from Schweizer et al., 2015.

avalanche speed accelerates to its maximum on the track before decelerating. In the runout zone, the deceleration of the avalanche is rapid, debris is deposited, and the avalanche stops (McClung and Schaerer, 2006).

## 2.3 Formation of avalanches

The formation of an avalanche is a complex interaction between three main contributing factors: terrain, meteorological conditions and physical parameters of the snowpack (Schweizer et al., 2015). The terrain is the only time-constant factor. Areas with a slope >30° are considered possible release areas for avalanches (Lied et al., 2003). Most slab avalanches occur in slopes between 35° to 45°, while dry loose snow avalanches occur between 30° to 60°. For steeper slopes, avalanches are rare. Avalanches in slopes less steep than 30° happen less frequently and are often wet avalanches (McClung and Schaerer, 2006). Other topographic attributes such as forest cover, aspect, curvature and roughness of terrain are other important factors in the formation of avalanches.

### 2.3.1 Meteorological conditions

The most important meteorological conditions contributing to avalanche formation are precipitation, wind, air temperature and solar radiation (Schweizer et al., 2015).

### Precipitation

Precipitation, in the form of new snow, is closely related to avalanche danger and is the strongest forecasting parameter. The probability of an avalanche increases with an increased precipitation rate, whereas the amount of new snow needed for an avalanche to occur differs depending on each situation. Snow storms are often critical, as heavy extra loading in a short time can lead to natural releases. Precipitation, in the form of rain, increases the probability of avalanches. The rain saturates the snowpack, leading to a decrease in cohesion and increased pore pressure and strain. Hence, rain can critically decrease stability in a short time. This can lead to wet avalanches forming on less steep slopes (Lied et al., 2003).

### Wind

Wind contributes to the transport and deposition of snow. Wind transports snow by rolling, saltation and suspension (Figure 2.3). The wind strength needed for snow drift depends on surface hardness and temperature. Less wind speed is needed for cold and soft surfaces. Snowdrift increases with the 3rd power of the wind speed (Lied et al., 2003).

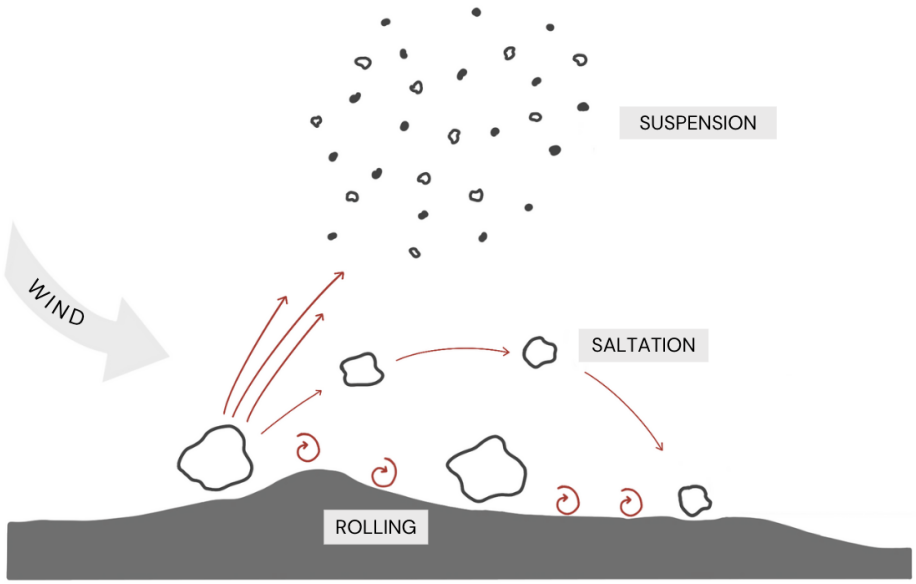


Figure 2.3: Illustration of wind-transported snow. Wind erodes the surface depending on wind speed, resulting in the transportation of snow particles: rolling (large snow particles), saltation (medium snow particles) and suspension (small snow particles).

#### Temperature and solar radiation

Temperature is the most decisive contributor to avalanche formation, as snow has low thermal conductivity. Changes in air temperature mainly affect the snow surface. An increase in air temperature after a storm may lead to snowpack instability by decreasing the stiffness of the slab while increasing the shear stress between the slab and the weak layer. Inside the snowpack, the rate of temperature change is important. A high-temperature gradient in the snowpack leads to kinetic crystal growth and the formation of weak layers. When the snowpack is exposed to warming leading to an increased snowpack temperature, instability factors happen immediately. Factors stabilizing the snowpack are delayed. This demonstrates how sensitive the avalanche formation is to temperature changes. Solar radiation contributes to surface warming. This will speed up the metamorphose of the snow crystals in favour of loose-snow avalanches (Schweizer et al., 2003).

### 2.3.2 Snowpack stratigraphy

The seasonal snowpack consists of layered snow that forms due to new snow, wind deposition and snow metamorphism within the snowpack. Each layer can be characterised by its thickness, crystal form and hardness. Snowpack stratigraphy is the key to the formation of dry slab avalanches. Additional loading and temperature increases will not affect the stability if the snowpack lacks existing weaknesses (Schweizer et al., 2003). Examination of the snowpack is necessary to discover weaknesses. Figure 2.4 illustrates an example of a snowpack stratigraphy assessment, called a snow profile. This way, properties of the different layers are assigned, and weaknesses are discovered.

## 2.4 Avalanche size classification

The Norwegian Avalanche Warning Services (NAWS) use the same avalanche size classification as the European avalanche warning services (EAWS). Avalanche sizes are classified from 1 to 5. Table 2.2 provides each size with descriptive characteristics.

Table 2.2: Avalanche size classification used by the Norwegian Avalanche Warning Services. An avalanche size is mainly classified by its damage potential.

| **Size** | **Description** | **Potential damage** | **Runout Classification** | **Path Length** | **Volume** |
|---|---|---|---|---|---|
| 1 | Small | Unlikely to bury a person | Stops within steep slopes | 10-30 m | $< 100\ m^3$ |
| 2 | Medium | May bury, injure or kill a person. Typical skier-triggered avalanche | May reach the end of the relevant steep slope | 50 - 200 m | $< 1000\ m^3$ |
| 3 | Large | May bury and destroy cars, damage trucks, destroy small buildings and break a few trees. | May cross flat terrain (below 30°) over a distance of less than 50 m | Several 100 m | $< 10{,}000\ m^3$ |
| 4 | Very large | May bury and destroy trucks and trains, may destroy fairly large buildings and small areas of forest | Crosses flat terrain (well below 30°) over a distance of more than 50 m. May reach valley floor. | 1-2 km | $< 100{,}000\ m^3$ |
| 5 | Extreme | May devastate the landscape and has catastrophic destructive potential | Reaches valley floor. Largest known avalanche | $> 2$ km | $> 100{,}000\ m^3$ |

## 2.5 Avalanche Forecasting in Norway

Avalanche forecasting is an important tool for mitigation of loss of life and property. A regional avalanche forecast service based on international standards was launched in January 2013 on Varsom.no. The service was developed in collaboration between NVE, MET, The Norwegian Public Roads Administration, Norwegian National Rail Administration and Norwegian Geotechnical Insitute (NGI), and is today operated by the first three (Müller et al., 2013).

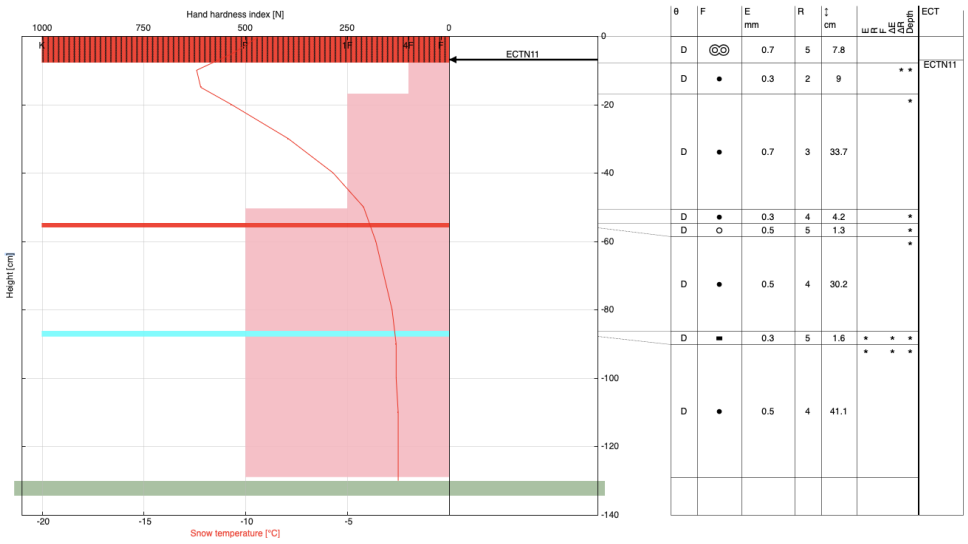


Figure 2.4: Example of a snow profile registered with Varsom RegObs. A weak layer is seen at 7.8 cm depth below a melt-freeze crust. An extended column test resulted in an initiated fracture in the weak layer (ECTN11). The temperature gradient is shown in a red line in y-direction. The right-sided panel shows the information on the crystal form, size, and depth of the layer. The field observation was done by M. Flaten on a field trip to Finse, Norway, March 2022. Altitude 1230 m.a.s.l., exposition East.

An avalanche forecast is created in a three-step process. First, snowpack- and weather data are collected to describe the present situation. Field observations are made and reported to RegObs by trained observers who assess the snow stability and the potential avalanche hazard. Then, weather forecasts are included to predict the influence on the current situation. Lastly, the avalanche danger is forecasted for 24 and 48 hours. The forecasts are issued daily on Varsom.no during the winter season and are updated when necessary based on changing conditions. The daily forecast contains the expected danger level for the region of interest, typical avalanche problems and exposed terrain. Avalanche danger is the potential for an avalanche to cause damage to something of value (Statham et al., 2018). The avalanche danger level is given as a number

between 1 and 5, from low to very high. An avalanche problem describes which structures of the snowpack and snow types are likely to release an avalanche and is an important factor in avalanche forecasts. The problems put context to the given danger level in a region, e.g., new snow, wind-drifted snow, persistent weak layers, wet snow and gliding snow. Both the avalanche danger scale and avalanche problems in Norwegian avalanche forecasting are based on European standards.

## 2.6 Remote sensing

Remote sensing is the process of obtaining information about an object or phenomenon from a distance. Various platforms, sensors, and resolutions characterize remote sensing systems. Generally, the platforms are categorized as ground-based, airborne or space-borne. Reflected and emitted radiation are measured by a sensor attached to a platform (e.g., a satellite or aircraft). This technology allows for monitoring and assessing changes in the Earth's surface without direct physical contact. The sensors can be passive or active. A passive sensor only measures the radiation naturally emitted by a target, e.g., an optical sensor. An active sensor emits and measures a target's reflected energy, e.g., LiDAR and Radar. An optical sensor depends on daylight and specific meteorological conditions to operate sufficiently. A radar covers the microwave region of the electromagnetic spectrum and operates on frequencies ranging from 300 MHz - 300 GHz (wavelength of 1 mm - 1 m) (Figure 2.5). This implies that radar signals can penetrate through clouds and thus operate despite any meteorological conditions (Lillesand et al., 2015).

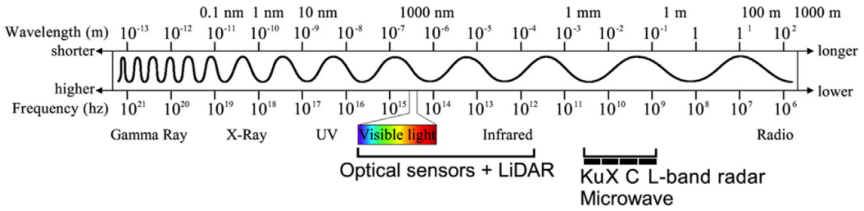


Figure 2.5: Figure of the electromagnetic spectrum with the range of frequencies and wavelengths of electromagnetic radiation. Optical sensors and LiDAR use the visible light and infrared ranges, while radars operate on the microwave range. Figure is obtained from Eckerstorfer et al., (2016).

### 2.6.1 Synthetic Aperture Radar

SAR is short for Synthetic Aperture Radar and is an imaging radar attached to a platform, i.e., a satellite. Signals are transmitted in sequences while the radar antenna receives the backscattered signals. As the satellite moves, the received signals construct a synthetic aperture longer than the physical antenna length.

This attribute allows SAR to be an imaging radar. The resulting radar image represents a measure of the reflectivity of a scene. SAR systems operate on different frequency ranges (bands) depending on the purpose. Penetration of the surface can occur at a certain level, depending on wavelength and frequency. The longer wavelength, the further it can penetrate, and the imaged media (e.g., vegetation, dry soil, ice and snow) can be seen as a volume. Examples of frequency bands and their applications are C-band; operating at 7.3-3.75 GHz with wavelengths of 4-8 cm, e.g., used for agriculture, ocean or ice monitoring and L-band; operating at 2-1 GHz and wavelengths of 15-30 cm, often used for foliage penetration and subsurface imaging. For high-resolution imaging, high frequencies are required (Moreira et al., 2013).

### 2.6.2 Geometric distortion in SAR images

Images of scenes with strong topography may be exposed to geometric distortions: e.g., foreshortening, shadow and layover (Figure 2.6). Foreshortening is due to the compression of backscatter in sensor-facing slopes. This happens when the signal is transmitted and received simultaneously, thus noting the same distance of the object. This results in narrow, bright bands being displayed in sensor-faced slopes. Layover occurs where mountains, high trees or buildings are in the way of the signal. The returned signal from the slope is received at the same as the return behind the slope, resulting in a "geometric flip" of the slope in the SAR image. Shadow often appears in areas behind mountains. This occurs when the angle behind the mountain is steeper than the incident angle, and the sensor cannot image the back. Shadows are seen as black features in the SAR image and contain no information (Weydahl et al., 2011).

## 2.7 Sentinel 1

The Sentinel-1 mission was developed by the European Commission (EC) and the European Space Agency (ESA) in the frame of The Global Monitoring for Environment and Security (GMES), today known as the Copernicus program (Torres et al., 2012). The goal was to offer free and openly accessible data for environmental and security monitoring. Sentinel-1 provides SAR imaging for different applications, including mapping of land surfaces, monitoring sea-ice, surveillance of marine environments and monitoring land surface motion risks (Attema et al., 2012). The mission consists of two satellites, Sentinel-1A and Sentinel-1B, launched in 2014 and 2016, each with an operational lifespan of seven years. Sentinel-1 operates in a near-polar, sun-synchronous circular orbit at 693km height and 98.18 degrees inclination. Each satellite has a 12-day repeat cycle at the Equator with 175 orbits per cycle (Eckerstorfer et al., 2018; ESA, 2023b). The two satellites map the global landmasses in the same orbit every 6 days. Sentinel-1 A and B carry a right-side-looking single C-band SAR

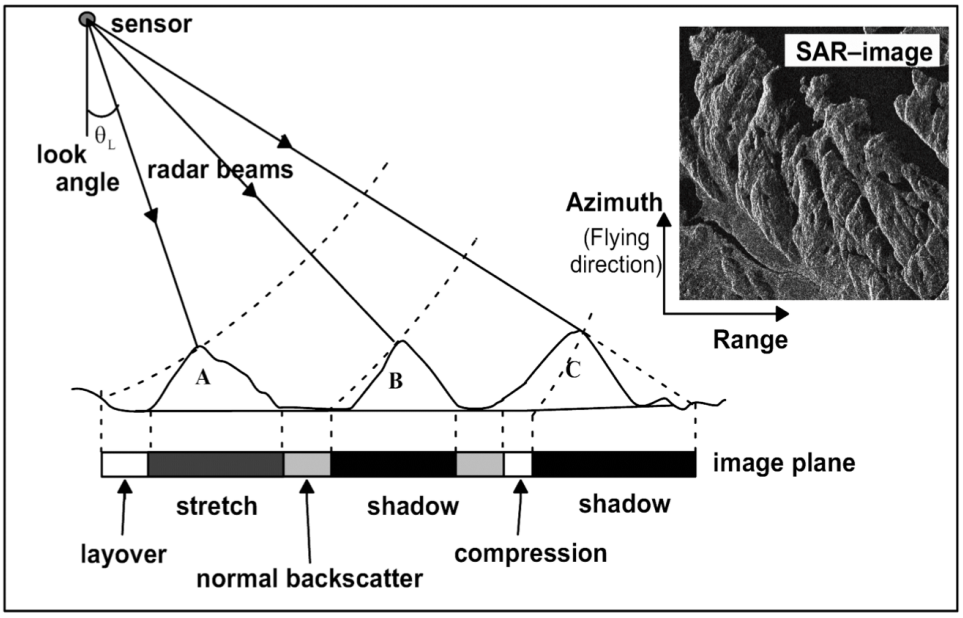


Figure 2.6: Illustration of geometric distortions in SAR images. The figure shows how layover, shadow and foreshortening (compression) may appear based on look angle and flying direction. The figure is obtained from Weydahl et al., (2011).

instrument operating with a centre frequency of 5.405 GHz and an incident angle range of 20-46 degrees (ESA, 2023c). As of today, Sentinel-1A is the only operational satellite. Sentinel-1B was considered lost in August 2022 after a failure affecting the power supply to the C-SAR antenna. Sentinel-1C will replace the operational span of 1B, and is planned to launch in the second quarter of 2023 (ESA, 2023a).

## 2.8 Avalanche detection in SAR images

SAR imaging for avalanche detection has been widely studied over the past decades. Space-borne SAR remote sensing was first introduced by Wiesmann et al., (2001). The study showed that increased backscatter in ERS1/2 SAR data resulting from rough, compacted avalanche debris could be used to detect a single avalanche. A change detection algorithm was constructed to identify the temporal change in backscatter between two SAR scenes; a reference image and an activity image intersecting as a RGB-composite. Martinez-Vazquez and Fortuny-Guasch (2006; 2008) were the first to show how ground-based SAR imaging could identify signatures of avalanches in the coherence image in two consecutive SAR images. An automated change detection scheme was developed by combining thresholding and morphological filters to a large

amount of differential coherence of consecutive SAR images. The possible candidates of avalanches were classified based on statistics extracted from the whole image and local characteristics.

Malnes et al., (2013) studied the performance of high-resolution Radarsat-2 Ultrafine Mode images on avalanche detection. Their results proved the possibility of visual identification of avalanche debris from single backscatter images due to high backscatter contrasts between debris and surrounding undisturbed snow. This was further studied in Eckerstorfer and Malnes (2015), where the researchers manually identified and classified 467 features as avalanche debris. Further, Landsat-8 optical remote sensing data and fieldwork validated 37% of the features as avalanches.

Malnes et al., (2015) were the first to demonstrate the potential for detecting avalanche debris in Sentinel-1A images. In their study they identified 489 avalanches by utilizing the relative backscatter change from a reference to an activity image. This was further studied in Eckerstorfer et al., (2017; 2022; 2019).

### 2.8.1 Detectability of avalanche debris

Radar backscatter quantifies how much of the signal is returned and measured by the sensor. The signal emitted from an active sensor will be reflected or scattered depending on the surface roughness. Figure 2.7 illustrates a scenario with three different surface roughnesses. For a smooth surface, the emitted radar signal will be totally reflected. With increasing surface roughness, the signal will be scattered. The rougher surface, the more signal will be backscattered and measured at the sensor. The backscatter coefficient is a measure of the returned signal. The signal can penetrate dry snow surfaces, but not wet snow surfaces (Weydahl et al., 2011). This affects the backscatter coefficient (Figure 2.8).

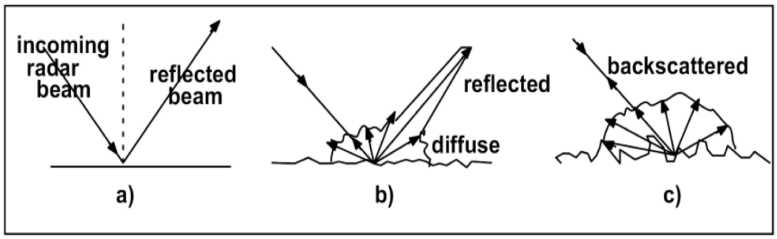


Figure 2.7: Illustration of how the backscattered signal increases with increasing surface roughness. In a) a totally, smooth surface is seen, leading to a total reflection of the signal, while b) and c) show increased surface roughness resulting in scattering of the signal and increased backscatter registered at the sensor. The figure is obtained from Weydahl et al., (2011).

Ulaby et al., (1986) provided a study of an electromagnetic model for undisturbed snow. Their results showed how the physical parameters of the snowpack, e.g., snow depth, snow density, crystal size, liquid water content and surface roughness, affected the total backscatter coefficient. The backscatter generated from the ground surface is the biggest contributor to dry snow. Backscatter generated at the air-snow interface and from volume scatter inside the snowpack also contributes to backscatter. The biggest contributor to backscatter for wet snow is the air-snow interface due to no penetration in the snowpack.

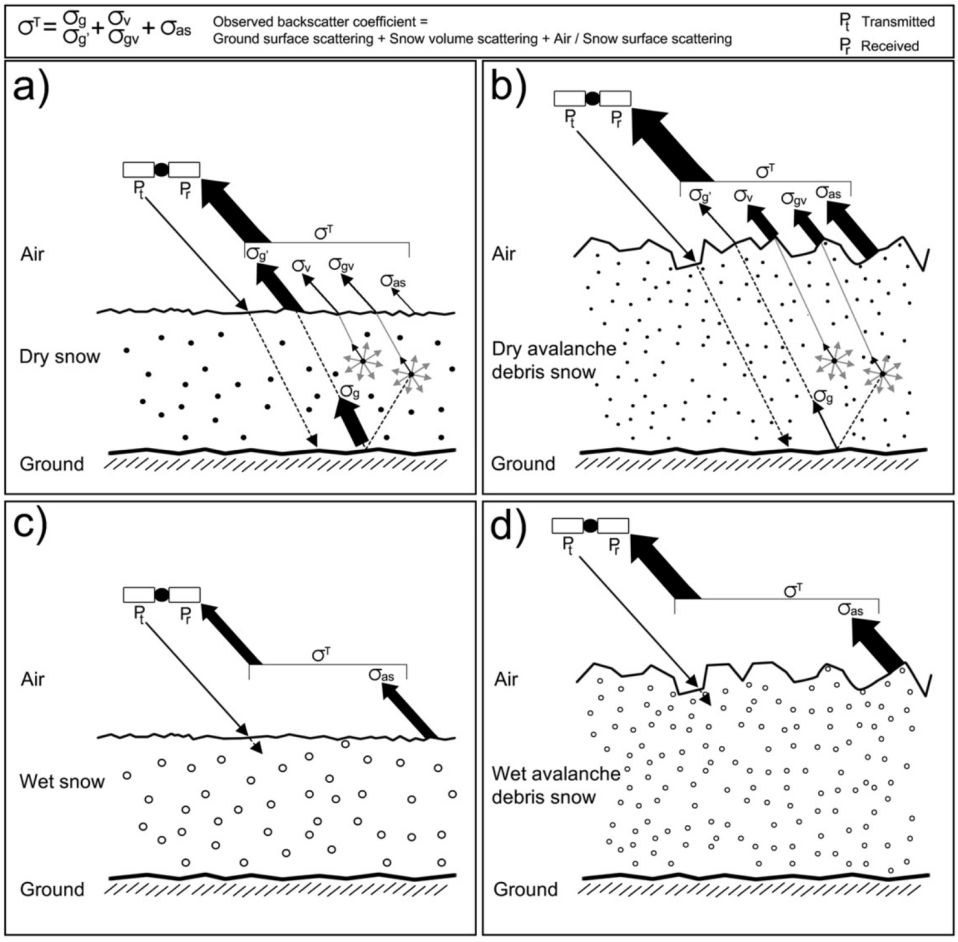


Figure 2.8: Qualitative model of the backscatter coefficient and its biggest contributors of a) dry, undisturbed snow, b) dry debris, c) wet, undisturbed snow, and d) wet debris, proposed by Eckerstorfer and Malnes (2015). The main contributors are a) ground surface scattering, b) air-snow surface scattering, c) air-snow surface scattering and d) increased air-surface scattering due to rougher surfaces. The figure is obtained from Eckerstorfer and Malnes (2015).

A similar model for disturbed snow (debris) is not yet fully studied. Eckerstorfer and Malnes (2015) proposed a qualitative interpretation of relative backscatter signals in dry and wet avalanche debris. Their study showed significantly different means between undisturbed and disturbed snow. The proposed model (Figure 2.8) is founded on the model for undisturbed dry and wet snow from Ulaby et al., (1986) and is based on the change in backscatter characteristics due to changes in the snow surface from undisturbed to disturbed snow. The theory for undisturbed snow is shown in Figure 2.8a and 2.8c. Figure 2.8b shows the case for dry avalanche debris. From increased volume backscatter (increased snow depth) and increased backscatter at the air–snow surface intersection (increased roughness), it follows an increase of the total backscatter coefficient ($\sigma^T$). In the case of wet avalanche debris, the roughness of the avalanche debris is likely to determine the total backscatter coefficient ($\sigma^T$).

Snow temperature is also shown to affect the backscatter. The study from Baumgartner et al., (1999) done on ground-based radars with C, X and Ku bands shows that snow with low-temperature results in higher backscatter compared to snow with high temperature. As stated by Vickers et al., (2016), images with wet snow are predicted to decrease backscatter relative to an image with dry snow.

### 2.8.2 Automatic avalanche detection algorithm

Eckerstorfer et al., (2017) presented a complete, two-year avalanche activity record from a Norwegian avalanche forecasting region using Sentinel-1 SAR images. The change detection method first introduced by Wiesmann et al., (2001) was used to combine two radar backscatter images of similar geometry and track into one RGB-composite. The reference image was used as input in the red and blue bands, while the activity image was used as input in the green band. As a result, an increase in relative backscatter appears as green features, while a decrease in relative backscatter appears as purple features. Avalanche debris was manually identified based on localised backscatter increase in runout zones. Manual identification of avalanche debris is time-consuming due to the high amount of data, and the development of an automated method was suggested.

Automation of the change detection method was further studied and developed in Vickers et al., (2016; 2017) and Eckerstorfer et al., (2019). Vickers et al., (2016) presented an algorithm based on the change detection method to identify potential avalanche debris. Further, the potential avalanches were classified as avalanche or non-avalanche pixels using the K-means unsupervised clustering method. The results showed a probability of detection (POD) over 60%, depending on chosen threshold, compared to manual detections. The algorithm was further developed in Vickers et al., (2017) to account for varying snow conditions in the Sentinel-1 images leading to different backscatter thresholds

for avalanche debris classification. The results did not show a significant improvement in POD but indicated a possibility for similar performance levels in larger detection areas influenced by changing meteorological conditions.

Further development of the algorithm was seen in Eckerstorfer et al., (2019). The K-clustering was replaced with a segmentation module combined with filtering to improve the detection results and process larger volumes of data. The results showed an average probability of detection of 64.7%., an average false alarm rate of 45.9% and a true skill score (TSS = POD-FAR) of 0.213. Today the algorithm outputs polygons, representing detected avalanches, with information on size, release time and time accuracy approximately 10 minutes after Sentinel-1 data is downloaded.

## 2.9 Limitations and sources of errors

The algorithm still needs improvement in order to work as an operational monitoring system. A transition from wet to dry snow conditions between the acquisition dates is known to be the biggest source for over-detecting of avalanches (Eckerstorfer et al., 2019). Wet snow has a lower backscatter coefficient compared to dry snow (Eckerstorfer and Malnes, 2015). As a result, the RGB-composite is composed of coherent green areas that may be detected as avalanche debris by the algorithm. In such a scenario, where air temperature changes from above to below freezing point, avalanche activity is less likely due to the assumed stabilizing of the snowpack. In Eckerstorfer et al., (2019), this was handled by manual deletion, which is not ideal when we aim for remote detection of avalanches. Another suggested source of falsely detected avalanches is changes in agricultural areas, man-made infrastructure, glaciers, debris flow channels and rock falls, as it is not possible to determine from C-band SAR data if an area consists of dry snow or no snow (Eckerstorfer et al., 2019).

The automatic change detection algorithm exhibits several points of limitation. Sentinel-1 SAR images have a pixel resolution of 20x20 meters. To reduce false alarms, a minimum of 10 pixels were used as a threshold for detections, limiting the detection possibility for small avalanches (Eckerstorfer et al., 2019). Further, avalanche detection is not possible in radar shadow and layover, which limits the attainable detection area in mountainous regions. Another major limitation is the availability of Sentinel-1 images. Due to the recent loss of Sentinel-1B, the availability of SAR images was reduced.

# CHAPTER 3

# Data and study area

## 3.1 Study area

We focused on data from the two forecasting regions Lyngen and Romsdal. Region Lyngen is located in the county Troms and Finnmark and covers Lyngen and parts of Tromsø municipality. The size of the region is 2157 $km^2$, whereas 604 $km^2$ consists of avalanche release zone (28% of the total area). Lyngen is well known by backcountry skiers for its many, high mountain tops, ranging from sea level up to 1841 m.a.s.l.

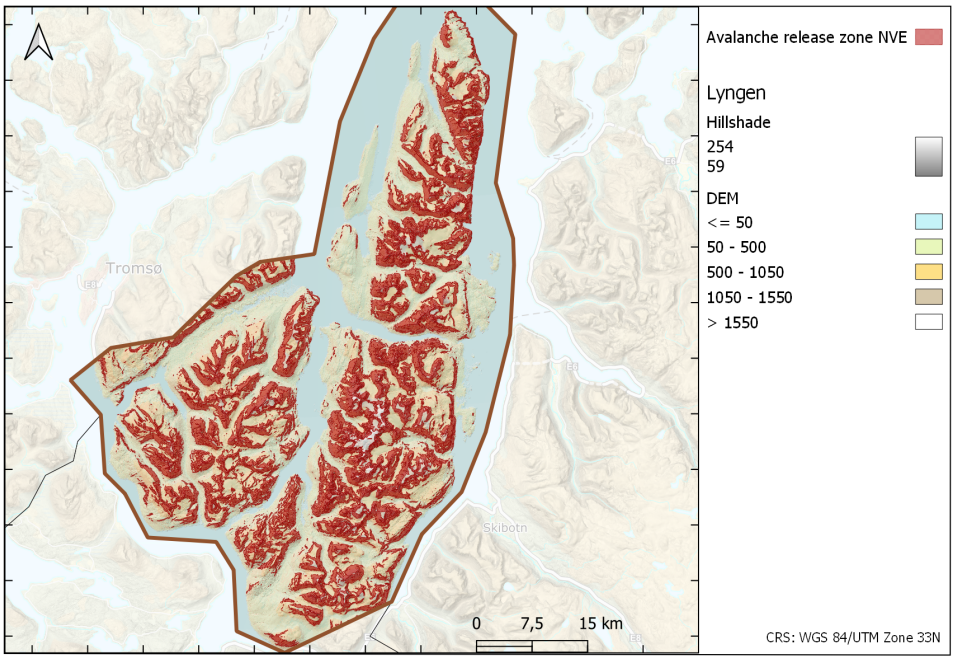


Figure 3.1: Map of the avalanche forecasting region Lyngen, located in Northern Norway. The avalanche release zone is highlighted in red.

Romsdal is located in Møre and Romsdal county. The size of Romsdal is 4462 $km^2$, with an avalanche release zone of 751 $km^2$ (16.8% of the total area). Romsdal ranges from sea-level up to 2002 m.a.s.l.

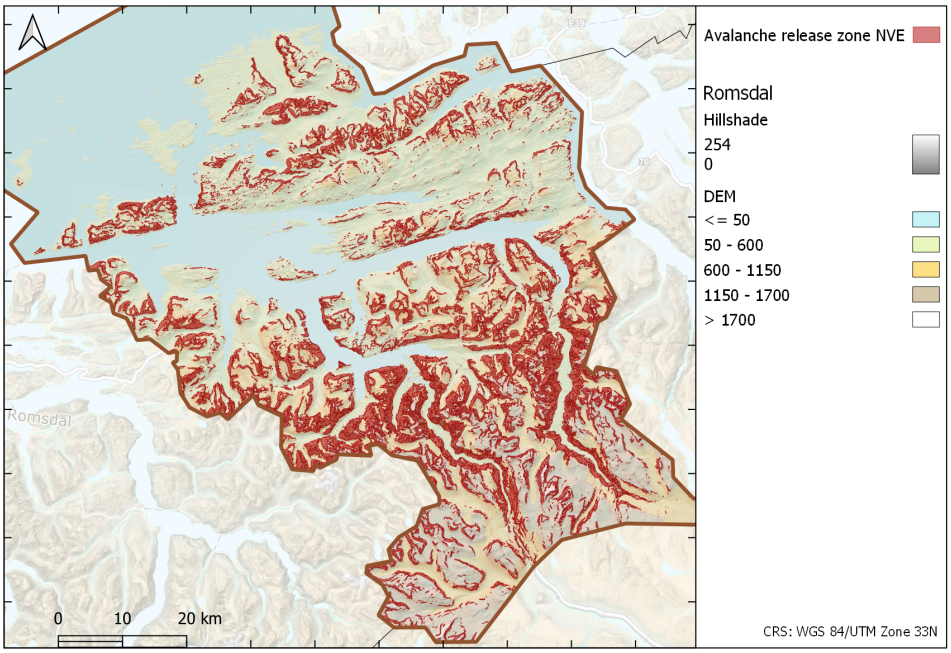


Figure 3.2: Map of the avalanche forecast region Romsdal, located in Western Norway. The avalanche release zone is highlighted in red.

## 3.2 Data access

The following subsections provide an overview of the data used in this thesis and how the data can be accessed.

### 3.2.1 SatSkred data

A geodatabase with exported SatSkred detections was provided by NVE. The geodatabase contained a shapefile with a total of 135999 spatially distributed polygons, each representing a potential avalanche debris detection in Norway from the winter seasons 2018/19, 2019/20 and 2020/21. Each polygon is described by several attributes, e.g., avalanche forecast region, registration time and size of the area. An overview of all attributes used for the description is seen in the Appendix (Table A1). Only detections from our two study regions, Lyngen and Romsdal, were considered in this thesis. An overview of the data can be seen in Section 3.4.

### 3.2.2 RGB composites

RGB-composites (also referred to as change detection images) covering Lyngen and Romsdal were provided by NVE. Each change detection image has a describing file name, including the reference and activity acquisition dates and track. Two examples of RGB-composites are seen in Figure 3.3 and 3.4. Original SAR images can be accessed through the Copernicus Open Access Hub.

### 3.2.3 Digital elevation model

A digital elevation model (DEM) with 10x10m pixel resolution for Lyngen and Romsdal was obtained by NVE. The DEM is a representation of the topographic surface of the bare ground.

### 3.2.4 Masks and maps

Multiple masks have been used in our QGIS analysis for both visual and practical consideration:

- **Basemap Norway:** used for navigation and visuals. Can be accessed from kartkatalog.geonorge.no
- **Susceptibility map:** raster layer containing mapped release and runout zones in Norway. Can be accessed from kartkatalog.geonorge.no (NVE)
- **Water and glacier masks:** Vector layers containing ocean and lake (Vanndirektiv kystvann og innsjø) downloaded from https://nedlasting.nve.no/gis/. Glacier mask obtained from NVE
- **Slope mask:** for visuals, obtained from NVE
- **Shadow mask:** for visuals, obtained from NVE
- **Cardinal direction mask:** for visuals, obtained from NVE

### 3.2.5 Meteorological data

Meteorological data were obtained from Varsom Xgeo. Varsom Xgeo is an expert tool for preparedness, monitoring and warning of floods, landslides and avalanches. Data from weather stations and models are compiled with events and field observations. Xgeo allows for viewing and downloading gridded weather data, both historical observations from weather stations, observation-based interpolated data and modelled weather data. For the interpretation of images as potential true or false detections, we chose to view weather data based on location. For our case studies, datasets containing air temperature (3 hours average), wind speed (3 hours average) and daily precipitation were downloaded for three altitudes in respective areas (Table 3.1).

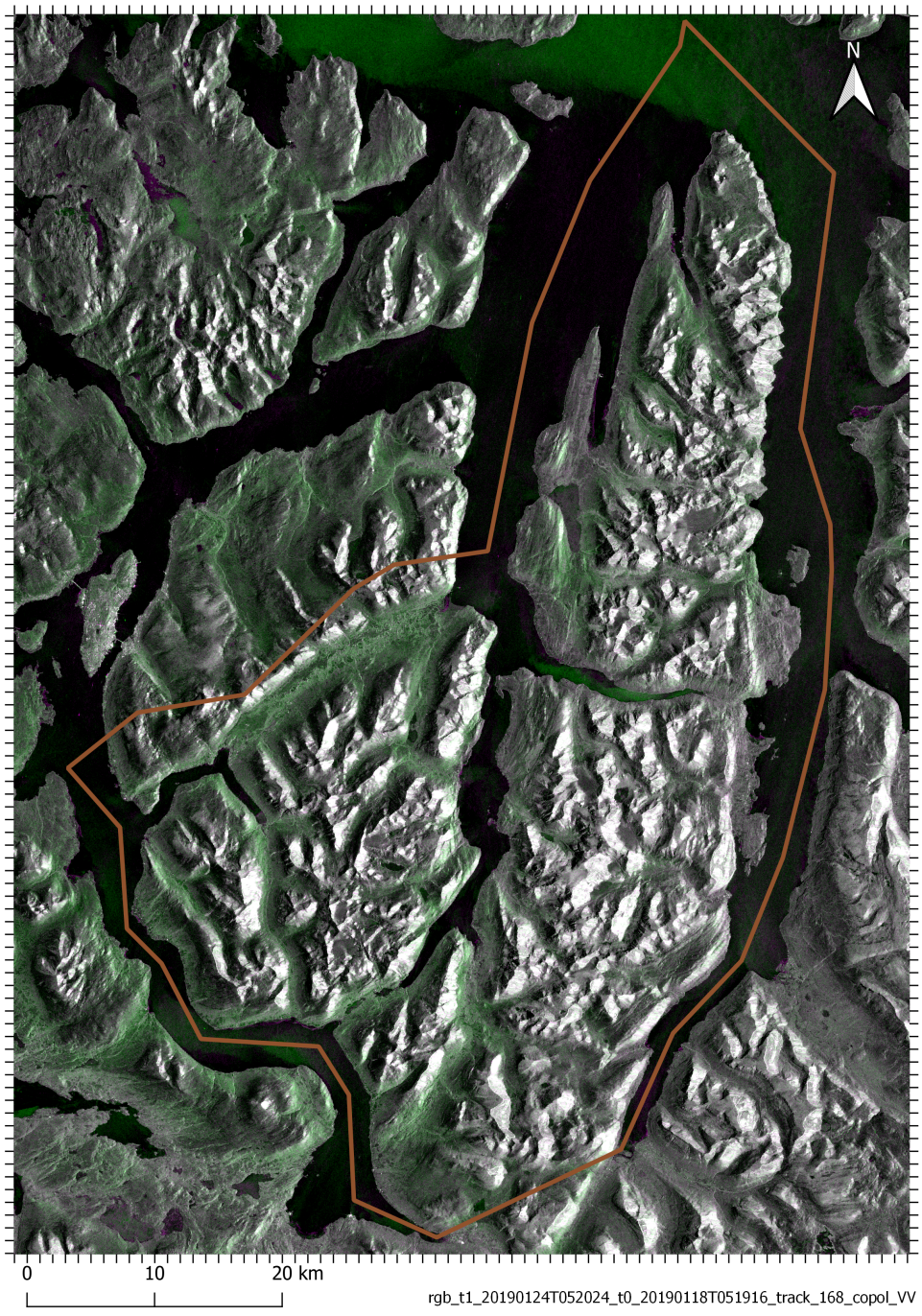


Figure 3.3: Example of a RGB-composite from Lyngen. The image shows contiguous green areas in the valleys, indicating increased backscatter. The change detection image was composed of SAR-images from 18. January 2019 (T0) and 24. January 2019 (T1) from track 168.

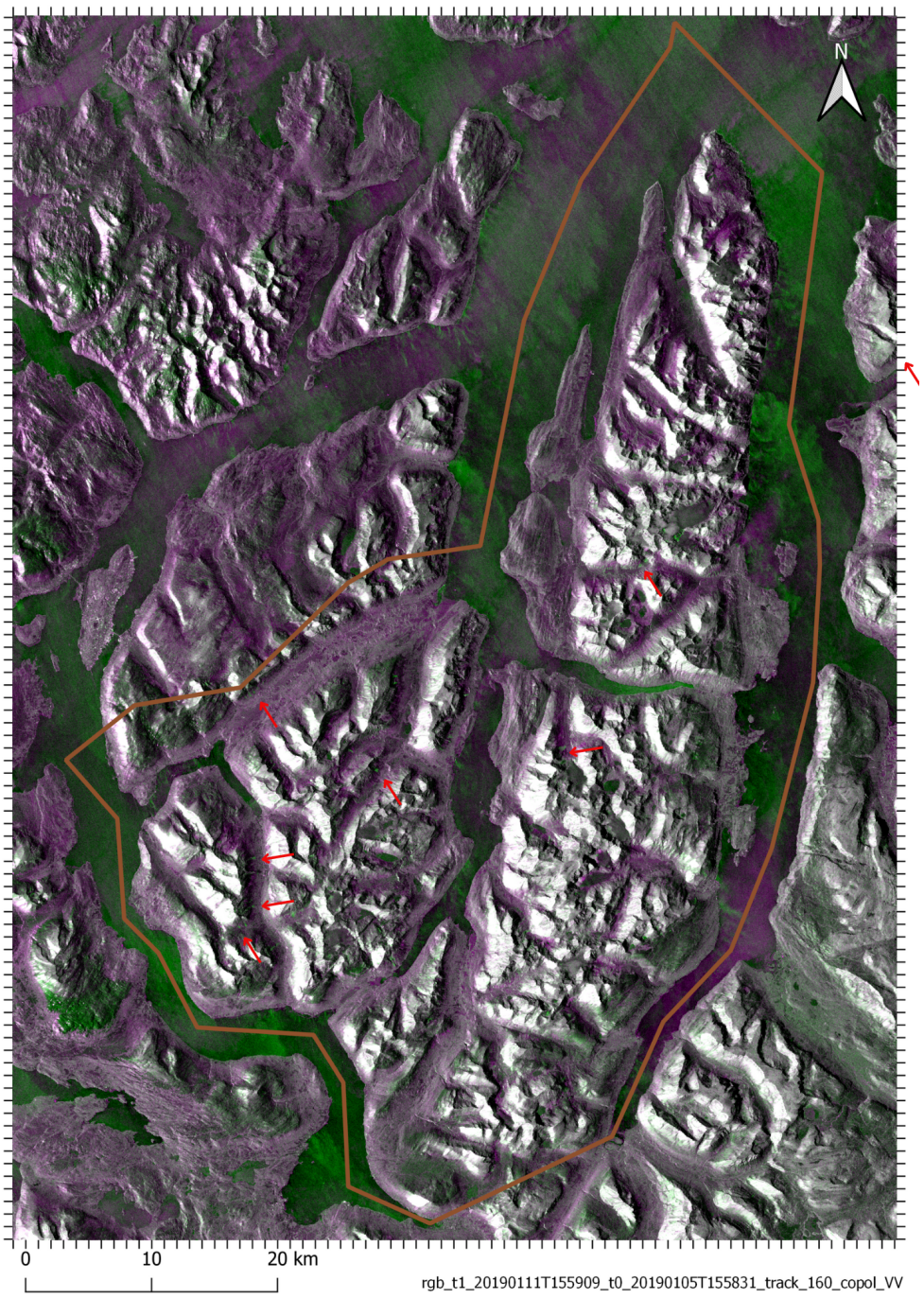


Figure 3.4: Example of a RGB-composite from Lyngen. The image is mostly purple in the valleys, indicating a decrease in backscatter. Green features are visible in multiple places, indicating potential avalanche debris (red arrows). The change detection image was composed of SAR-images from 5. January 2019 (T0) and 11. January 2019 (T1/) from track 160.

Table 3.1: Altitudes and coordinates for weather data obtained from Xgeo, used in case studies. Coordinates with reference from UTM zone 33N.

| Area | Altitude (masl.) | Coordinates (X,Y) |
|---|---|---|
| L1 | 32 | 667758,7703740 |
| L1 | 671 | 665133,7707868 |
| L1 | 1244 | 663504,7710344 |
| R3 | 135 | 122451,6952555 |
| R3 | 687 | 126324,6952840 |
| R3 | 1685 | 126578,6946617 |

## 3.3 Software

### 3.3.1 Python

Python is a free, general-purpose programming language. In this study, Python was used for the analysis of datasets and the creation of plots. Python version 3.10.10 was used. All codes and other data regarding the thesis are made available on github.com/NVE/satskred/tree/master/greenness. The following packages were used:

- `NumPy` for mathematical operations
- `pandas` for data analysis and manipulation tool
- `matplotlib` for creating plots and visualisation of data, mostly editing the already plotted data by fixing the plots
- `seaborn` for creating plots and visualisation of the data

### 3.3.2 QGIS

QGIS (previously known as Quantum GIS) is a free, open-sourced geographical information system. It allows for creating, editing, visualising and analysing geospatial data for both vector- and raster data. QGIS was used for analysing and interpreting of RGB-composites, zonal greenness analysis and creation of maps. For this study QGIS version 3.24.2 was used.

## 3.4 Description of dataset

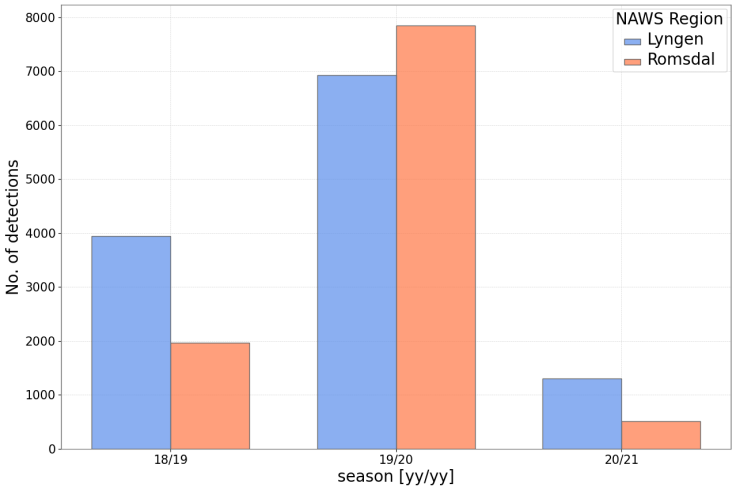


Figure 3.5: Distribution of detections per season, separated by region. The season with the most detections was the season 2019/20.

The dataset of automatically detected avalanches (hereafter detections) contained a total of 22475 detections from Lyngen and Romsdal. The detections were distributed over the three winter seasons 2018/19, 2019/20 and 2020/21, with a total of 12163 and 10312 detections in Lyngen and Romsdal, respectively (Figure 3.5).

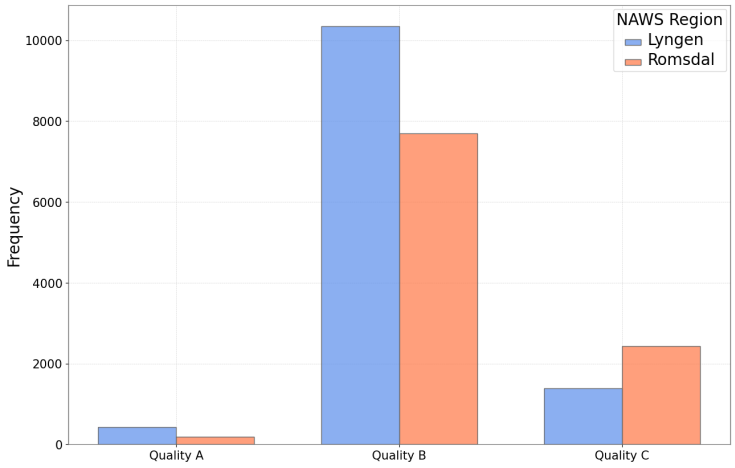


Figure 3.6: Distribution of acceptance quality in dataset, separated by region. Most detections have acceptance quality B, while the fewest have acceptance quality A.

.

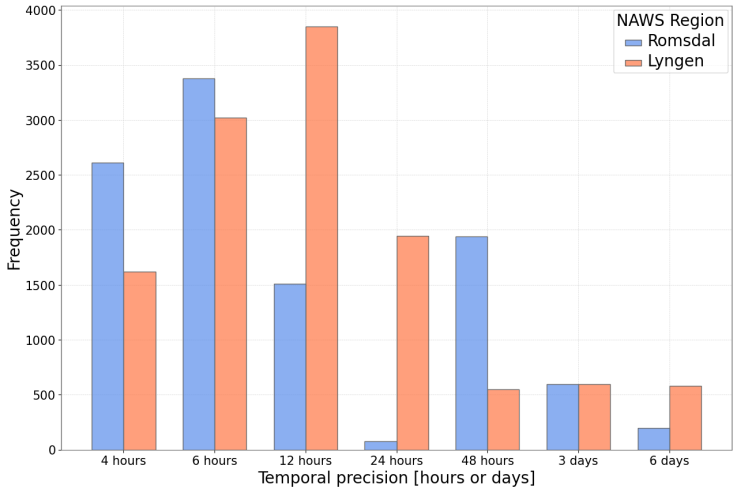


Figure 3.7: Distribution of temporal precision for detections in Lyngen and Romsdal. 71% of the dataset has a temporal precision equally or below 12 hours.

.

Each detection was registered with a quality A, B or C by the automatic change detection algorithm based on different criteria in a test filter. Quality C was used for detections flagged with river, >= 30% glacier, >= 20% agriculture, >= 20% urban areas or a temporal precision of 48 hours or more. Quality B was used for detections with better conditions than quality C but without overlapping with a known avalanche path. Quality A was used for detections with better conditions than quality B, meaning some overlapping with a known avalanche path in the detected area. Figure 3.6 shows that the most frequent acceptance quality of the detected features was "Quality B". A potential detection was removed if the detected area consisted of over 95% glacier or agriculture.

The temporal precision describes the time from the avalanche release to the registration date. Figure 3.7 shows that a precision of six hours was most frequent in Romsdal, while 12 hours was the most frequent in Lyngen. The distribution of the detection area is visualised in Figure 3.8. The distributions of slope and elevation of detections are seen in Figure 3.9.

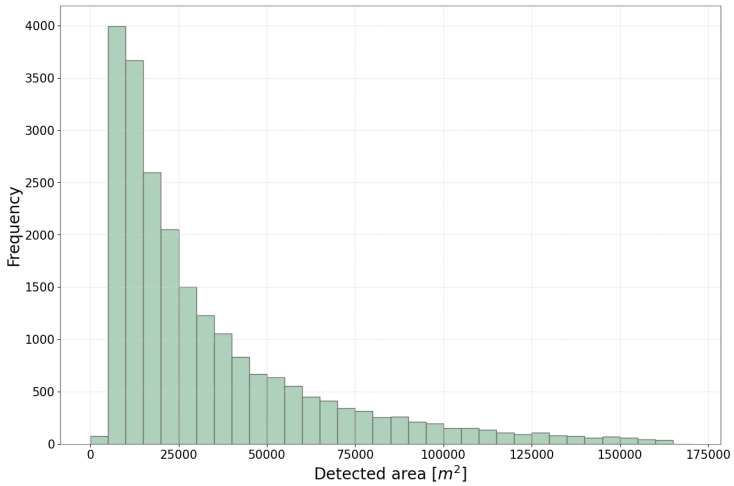


Figure 3.8: Distribution of detection area. Bin size = 5000 $m^2$. The histogram shows a left-skewed peak at 10000 $m^2$. The mean detection area is 33647 $m^2$. The median detection area is 22095 $m^2$.

The distributions of the number of detected avalanches in Lyngen and Romsdal are seen in Figure 3.10 and 3.11, respectively. When a feature was detected and accepted as avalanche debris, it was registered with two-time stamps; the registration date and the avalanche date. The registration date refers to the date and time of the activity image, T1. The algorithm estimates the avalanche release date by taking input from other available S1-images of similar tracks between T0 and T1, looking for changes in temporal backscatter. Suppose an

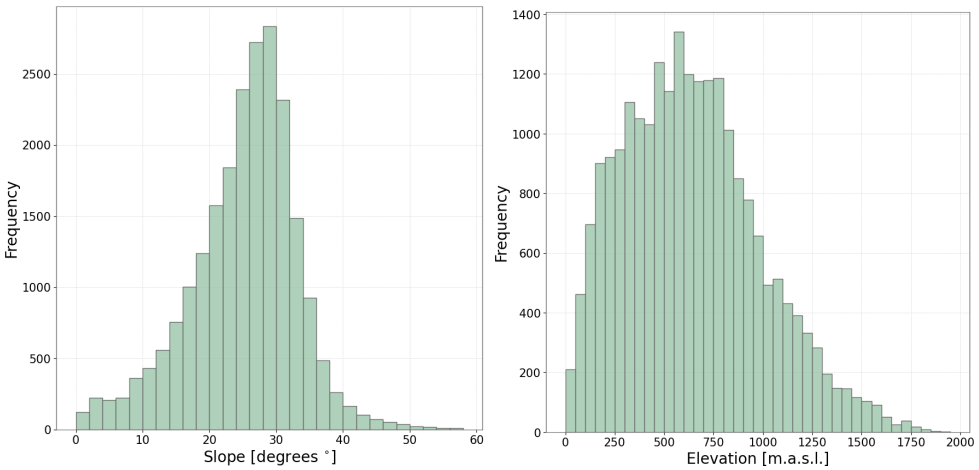


Figure 3.9: Left: Distribution of mean slope for detections in the dataset. Bin size = 2. Right: Distribution of altitude for detections in dataset. Bin size = 50.

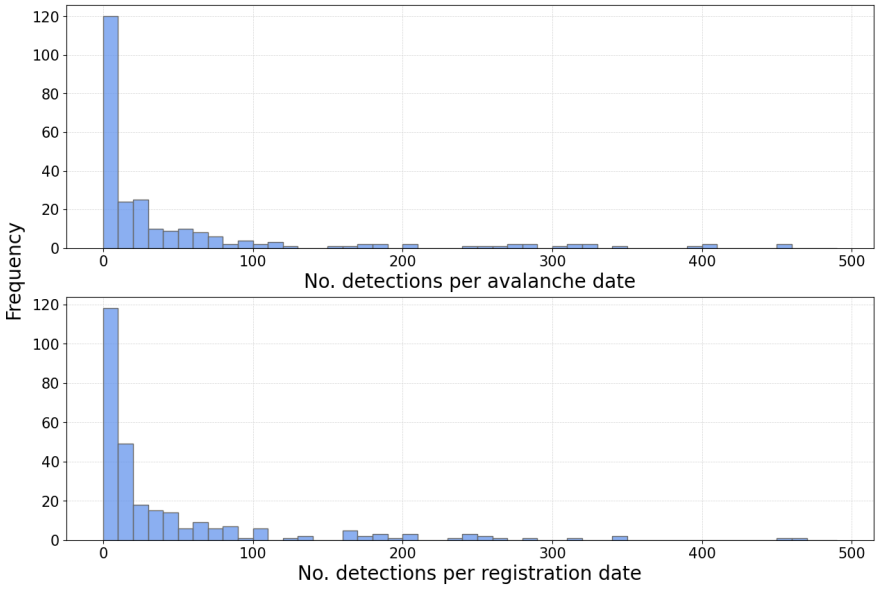


Figure 3.10: Distribution of detections in Lyngen. Bin size = 10 detections. A peak is seen in the first bar of both figures. Top: Distribution of detections per estimated avalanche release date. Bottom: Distribution of numbers of detections per acquisition date.

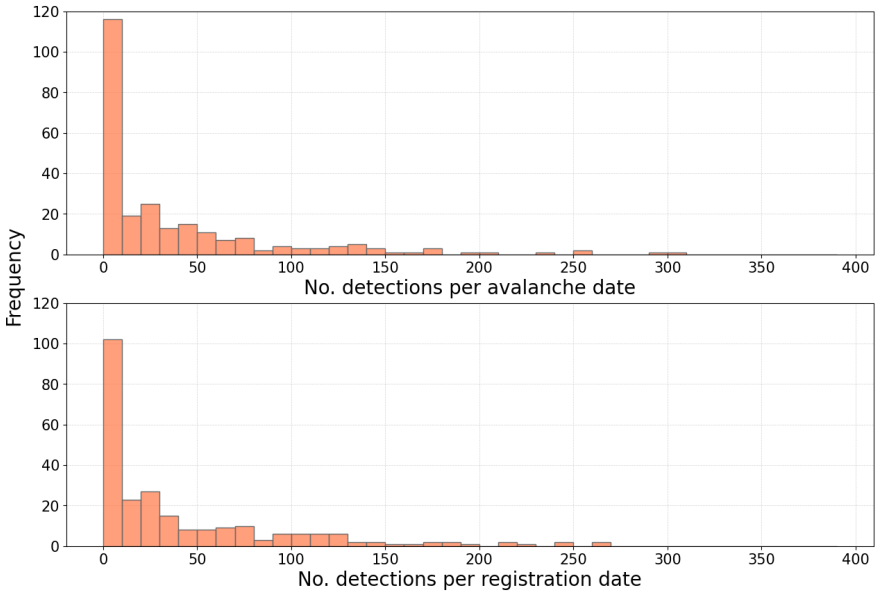


Figure 3.11: Distribution of detections in Romsdal. Bin size = 10 detections. A peak is seen in the first bar of both figures. Top: Distribution of detections per estimated avalanche release date. Bottom: Distribution of the number of detections per acquisition date.

image from a crossing track did not exhibit the change in backscatter as seen between T0 and T1. In that case, its timestamp would be used as a reference for the avalanche date, with a temporal precision depending on the time frame between the avalanche date and T1. This way, the time of the avalanche is excluded within the first time frame, between T0 and the avalanche date.

Table 3.2 provides statistics of the number of detections in Lyngen and Romsdal, per change detection image. The dataset containing detections from Lyngen originates from 279 RGB-composites. The maximum number of detections in one image was 468, with a median of 12 and a mean of 43.59 detections. Likewise, the dataset for detections in Romsdal originates from 247 RGB-composites. The maximum number of detections in one image was 269, while the median and mean is 19 and 41.75, respectively. For further analysis in this thesis, we will inspect images with "many" detections. As seen in Chapter 4, we have chosen to inspect change detection images containing the top 15% of all detections. This threshold is 84.3 and 96 in Lyngen and Romsdal, respectively.

Table 3.2: Statistics of the number of detections per acquisition date in Lyngen and Romsdal

| | Lyngen | Romsdal |
|---|---|---|
| Count | 279 | 247 |
| Min | 1 | 1 |
| Mean | 43.59 | 41.75 |
| Standard deviation | 74.54 | 55.29 |
| Median | 12 | 19 |
| 85% | 84.3 | 96.0 |
| Max | 468 | 269 |

# CHAPTER 4

# Method

## 4.1 Quantification of backscatter: Greenness Indicator

As explained in Section 2.8.2, a RGB-composite is composed of two radar images with similar geometry and track; the reference image is input in the red and blue bands, and the activity image is input in the green band. Pixels exhibiting a relative increase in backscatter will appear as green, while pixels exhibiting a relative decrease will appear as purple. If there is no change in backscatter the pixel will appear grey. Each individual pixel has values from the red, green and blue bands, each ranging from 0-255. Specific weather conditions can also lead to an overall increase or decrease of backscatter relative to the reference image, thus the whole image will be affected by green or purple colours (Section 2.8.1).

We hypothesise that how "green" a specific area in a RGB-composite is can predict of whether the detections are potentially true or false. We aimed to develop a quantification and simplification of the raster band values in the composed RGB images, a so-called *Greenness Indicator*. Inspired by the normalised difference vegetation index, the following Greenness Indicator method was put forward (Equation 4.1).

$$GI = \frac{band_G - band_B}{band_G + band_B} \tag{4.1}$$

The GI is calculated for each pixel in a RGB-composite using the raster calculator in QGIS, transforming each pixel and its band value to a number between -1 and +1. Zero equals no change in backscatter, -1 to maximum negative greenness (decrease in backscatter) and +1 to maximum positive greenness (increase in backscatter). Thus, the higher increase of relative backscatter, the higher value of GI. With this approach, we can explain how "green" a defined geographical area in a RGB-composite is, i.e., how much the relative backscatter has changed.

## 4.2 QGIS: Zonal greenness analysis

In the previous section, an approach combining backscatter values from the reference and activity image was proposed. Our hypothesis states that we should see an increase in greenness from both non-avalanche terrain to avalanche terrain and from avalanche terrain to detection area. We conducted a zonal greenness analysis in QGIS to explore this hypothesis among potential true and potential false (positive) detections in a selection of RGB images with "many" detections. This section describes the methodology in each step of the zonal greenness analysis.

### 4.2.1 Selection of RGB-composites

To establish a threshold for "many" detections in a RGB-image, several approaches have been considered. In our dataset, the detections originate from in total 247 and 259 RGB change detection images in Romsdal and Lyngen, respectively. In the following analysis, we have decided to consider and inspect RGB-composites containing the top 15% of detections as many detections. Based on this, the threshold for many detections are 96 and 84 (Table 3.2). From Table 4.1 we see that the top 15% of the RGB-composites contain a total of 5901 and 8040 detections in Romsdal and Lyngen, respectively, equal a coverage of 57.2% and 66.1% of total detections in the SatSkred dataset.

Table 4.1: Table illustrating the coverage of total detections in the dataset by inspecting the top 15% of images containing the most detections. The selected threshold covers 57% and 66% of the total detections in Romsdal and Lyngen, respectively.

| | Lyngen | Romsdal |
|---|---|---|
| No. RGB-images | 279 | 247 |
| No det. total | 12163 | 10312 |
| No det. top 15% | 8040 | 5901 |
| % of dataset | 66.10 | 57.22 |

Eight change detection images were selected and analysed from each region, chosen from the upper and lower boundaries of images with many detections. The in total of 16 RGB-composites are listed in the Appendix (Table A2.)

### 4.2.2 Areas

To account for local variations of detectability in RGB-composites covering the regions, we decided to split up the regions into smaller areas. A total of 12 polygons, six in each region, were drawn randomly in areas with many visible detections in QGIS. The resulting smaller areas can be seen in Figure 4.1.

Each polygon represents a smaller area of a maximum of 20 x 20 km within the respective region. The sizes of each area can be seen in Table 4.2. By choosing to inspect smaller areas, we will get more data points originating from the same change detection image, as well as having the ability to interpret separate parts of a RGB-composite as a potentially true or false detection. For an overview of the number of detections in each smaller area, see Appendix (Table A3).

Table 4.2: The size of areas L1-L6 and R1-R6. The largest area is L1 in Lyngen, while the smallest is R6 in Romsdal.

| **Area** | **Size** [km$^2$] |
|---|---|
| L1 | 279.4 |
| L2 | 186.2 |
| L3 | 129.4 |
| L4 | 230.4 |
| L5 | 138.2 |
| L6 | 99.3 |
| R1 | 271.8 |
| R2 | 168.9 |
| R3 | 244.6 |
| R4 | 217.7 |
| R5 | 201.9 |
| R6 | 48.4 |

### 4.2.3 Zones

Four zones were created in each area to prepare for zonal greenness analysis:

- Zone 1 = NONE: Non-avalanche terrain
- Zone 2 = AT: Avalanche terrain
- Zone 3 = DET: Automatic detected avalanche debris
- Zone 4 = B40: Buffer zone around the automatically detected avalanche debris

NONE was created by subtracting the avalanche runout- and water/glacier mask from the area polygon. The zone covers flat areas without overlying release areas. AT was created by cropping the avalanche runout mask to the smaller area polygons, resulting in one zone for each area with only the avalanche terrain. NONE and AT will in this part of the analysis be considered stationary zones, as they do not change depending on each individual RGB-composite. DET was created by cropping the vector files containing the

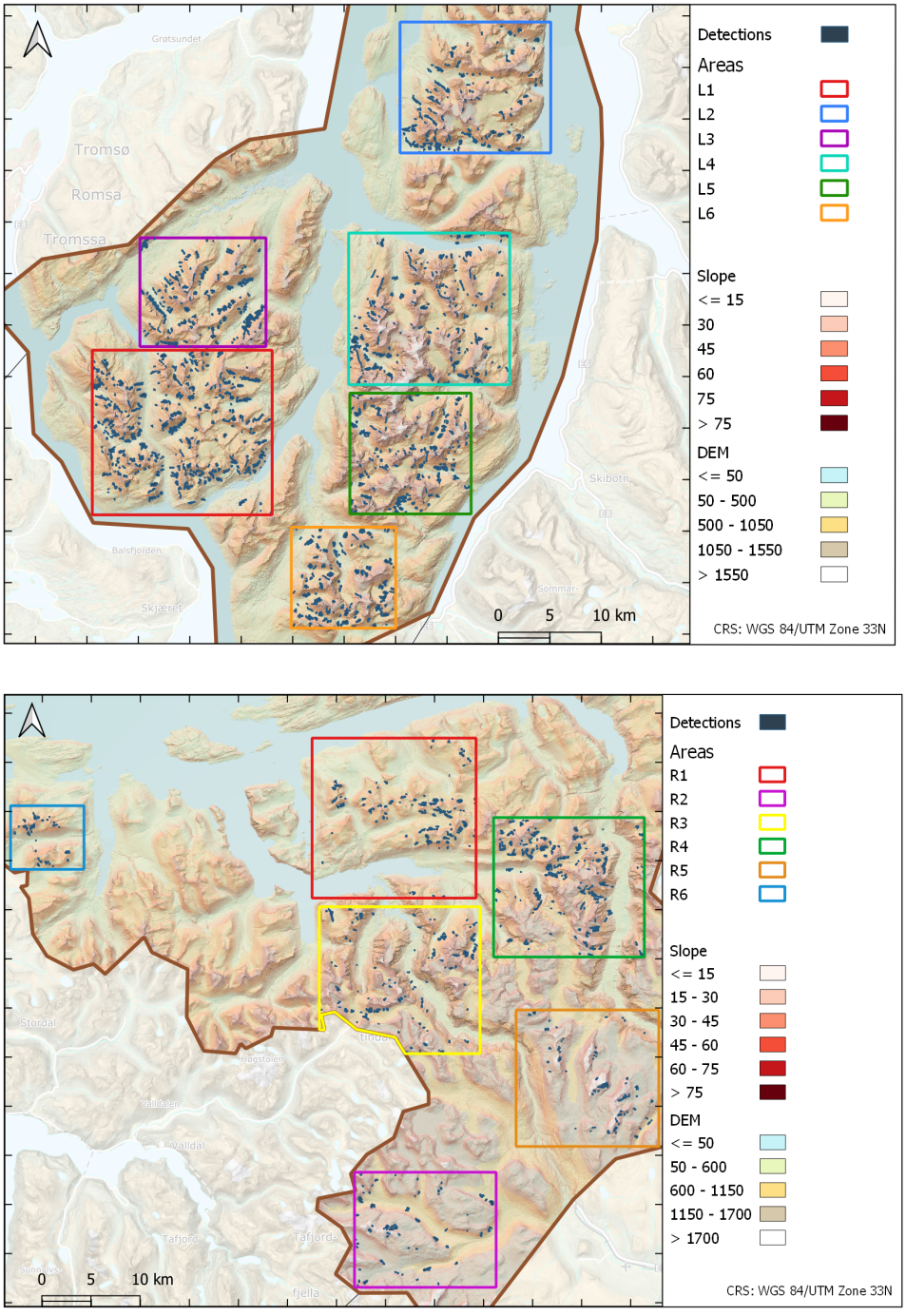


Figure 4.1: Map of the in total 12 selected areas in Lyngen and Romsdal. Top: Lyngen, area L1 - L6. Bottom: Romsdal, area R1 - R6. Green features inside each area represent the detections from the selected RGB-composites in the zonal greenness analysis (Table A3).

detection polygons. This was done on vector files with detection polygons separated by registration date. The resulting DET-zones mark the areas for detections in each RGB-composite.

B40 was decided to be a buffer zone with 40 meters width around the detection polygons. We wanted the buffer zone to be statistically similar in size with DET (Figure A1, Table A4). By choosing 40 meters width, we got a surrounding buffer area of 2 pixels (relative to the RGB-composites). The buffer (including DET) was created by the QGIS tool "Buffer", chosen to have a 40 meters width and the rest of the default settings. Further, a subtraction of DET was done to ensure B40 just as an outline of the detections. DET and B40 are also included in AT. An example of zones from area L4 in Lyngen is shown in Figure 4.2.

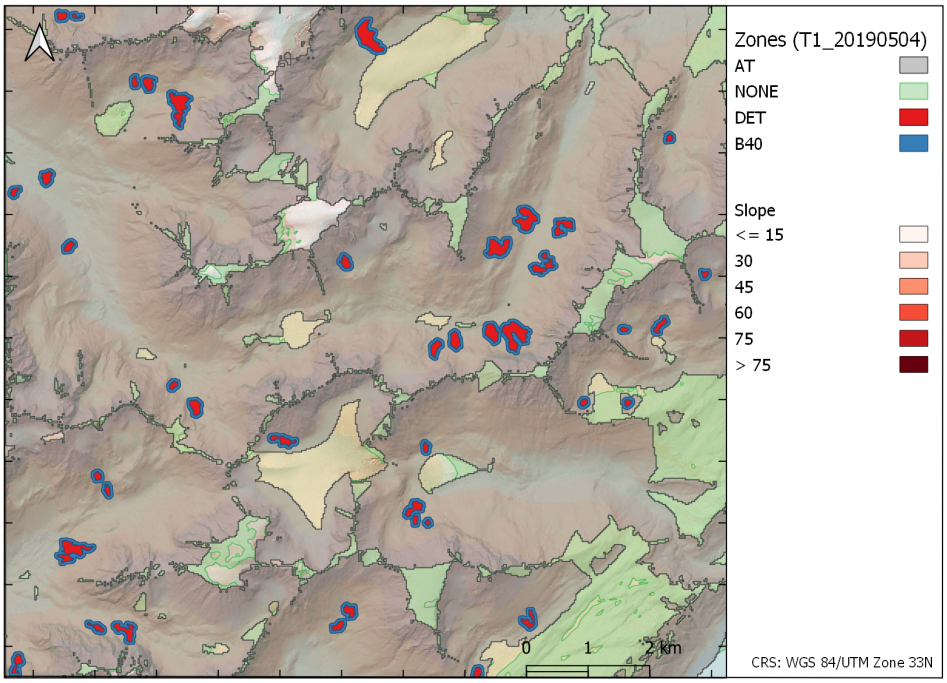


Figure 4.2: Example from L5 illustrating the four zones. DET and B40 are from the RGB-composite with activity reference 04/05/2019 16:07 (Table A2).

### 4.2.4 Interpretation of RGB change detection images

Smaller areas of the RGB-composites have been interpreted as a potentially true or false detection. Firstly, the change detection image itself was analysed for local differences. Similar trends were seen in most of the selected images. Following, an interpretation was based on how each RGB-composite looked. Some were clearly either true or false, others more unsure. Weather data from Varsom Xgeo and observations from RegObs were used to confirm the

interpretation from the RGB-image or help interpret the unsure ones. Results from interpretation analysis for each specific area and image can be viewed in the Appendix (Table A5, A6). The following two examples show the interpretation of 11/12/2019 16:15 in area L1, Lyngen, and02/04/2019 17:11 in area R4, Romsdal.

### Example 1: Potential false detection

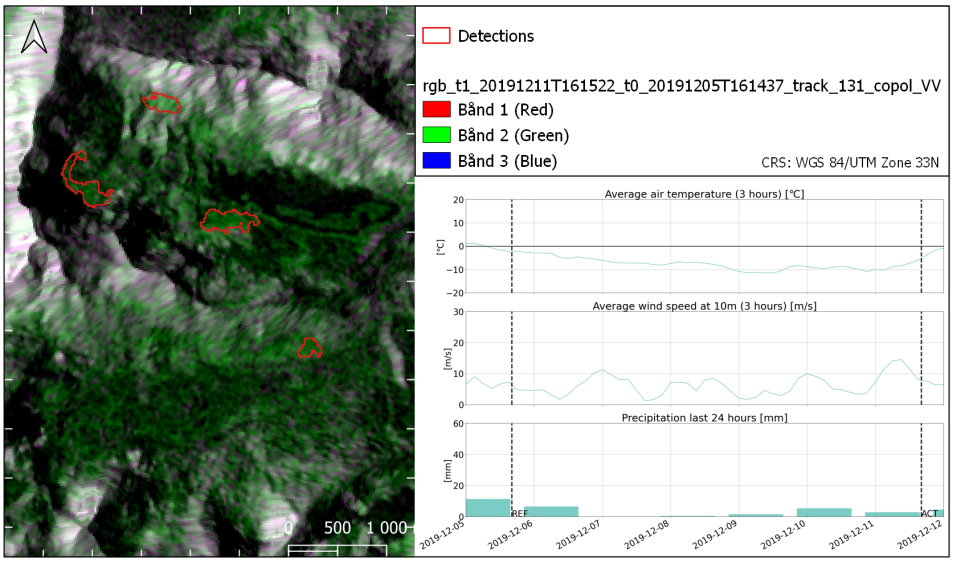


Figure 4.3: Example of potentially false detections, North-East in L1. Red outlines show bright, green features without clear contrast to the surrounding area. Weather data from 671 masl. indicates below-freezing temperatures at both acquisition dates, but transitioned from above to below freezing temperatures on the day of the reference acquisition date. Some new snow fell on the day and the day before the reference acquisition date.

The example shows a "green" image with no clear contrast between the detected and surrounding area (Figure 4.3). The temperature transitioned from above to below zero earlier on the day of the reference acquisition date, and we believe that the snow surface may still be wet, at least for lower altitudes. According to RegObs, no observations of avalanches and instability have been seen between the acquisition dates. This detection scenario is interpreted as false based on the RGB-composite and a possible transition from wet to dry snow surface.

### Example 2: Potential true detection

The second example shows a more purple change detection image (Figure 4.4). Here the detections are more visible as green features with high contrast

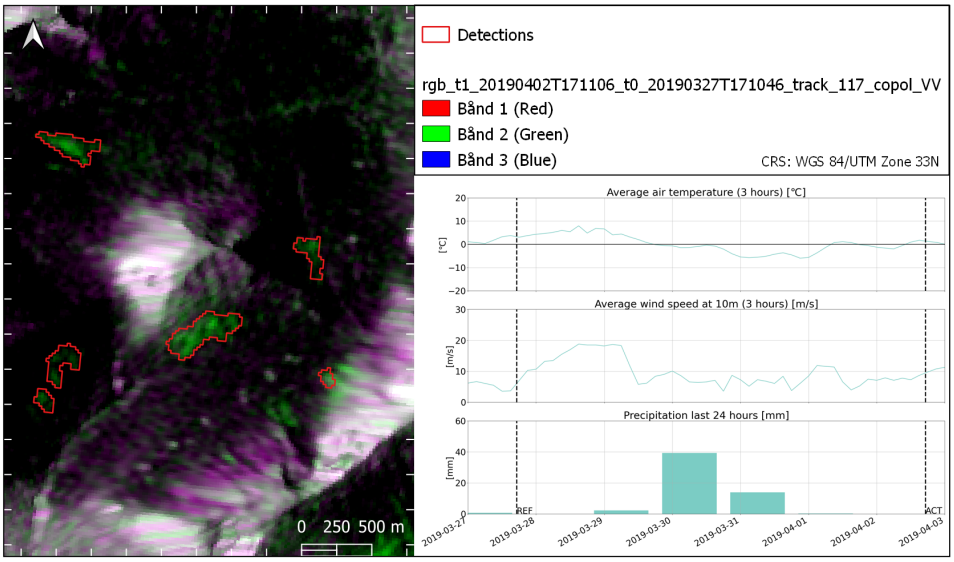


Figure 4.4: Example of potentially true detections, North-West in R4. The red outlines show bright and green detections in high contrast to the surrounding areas. The temperature was above zero on both acquisition dates. A period of warmer temperatures together with a heavy new snow event is seen in the first days after the reference acquisition date.

to surrounding purple pixels. Large amounts of new snow after a day with warm weather and snow melt are known to contribute to avalanche activity. Furthermore, RegObs reported of unstable snow due to persistent weak layers and observations of avalanches, which confirms the overall picture. Based on how the change detection image looks in the areas of investigation, weather data and snow observations, these detections are classified as potentially true.

### 4.2.5 Zonal statistics

The plugin Zonal Statistics in QGIS can be used to analyse the statistical results of a thematic classification. This allows for calculating several statistical values of the pixels of a raster layer within a polygonal vector layer. Chosen statistics were count (number of pixels containing a value) and sum (pixel greenness sum inside a polygon). Outputs of the zonal statistics were saved as .csv files with specific names for area, zone and image, for further formatting.

## 4.3 Formatting of results

Vector layers contain multiple features (e.g., multiple detection polygons or buffer zones). The zonal statistics were calculated individually for each feature. An algorithm was used to add the total count and sum, and further calculate

the mean zonal greenness for each .csv file. Each resulting mean zonal greenness was stored in a DataFrame (hereafter referred to as the dataset). Each row in the dataset represents the results from an area within a RGB-composite. In the columns, the interpretation of the data point as true or false, mean greenness values in the four zones (NONE, AT, DET and B40) and the mean greenness contrasts (AT-NONE, DET-AT, DET-B40 and B40-AT) were stored.

### 4.3.1 High-influential data points

With six smaller areas and a total of 8 RGB-composites in each region, the initial number of rows in the dataset was 96. A total of six areas consisted of zero detections in DET, and the rows were further removed. During the analysis, we experienced complications with data points exhibiting low pixel count in DET, indicating few detections. Figure 4.5a illustrates how greenness and pixel count varies a lot within the same image, region and area. The figures indicates that when comparing mean greenness in zones, data points originating from just a few detections can be problematic and skew the results.

Our dataset contains several points which originate from just a few detections, mainly in R2, R5 and R6 (Table A3). Figure 4.5b shows the distribution of pixel count in DET from our analysis dataset. The figure shows a left-skewed distribution with high variation of data points based on pixel count. To avoid this problem, we have excluded data points with pixel count below the lower quartile ($< 25\%$). The cutoff threshold is at 751.5 pixels (Table A7), which equals a detection area of 0.3006 $km^2$ at a 20 x 20 meters pixel resolution.

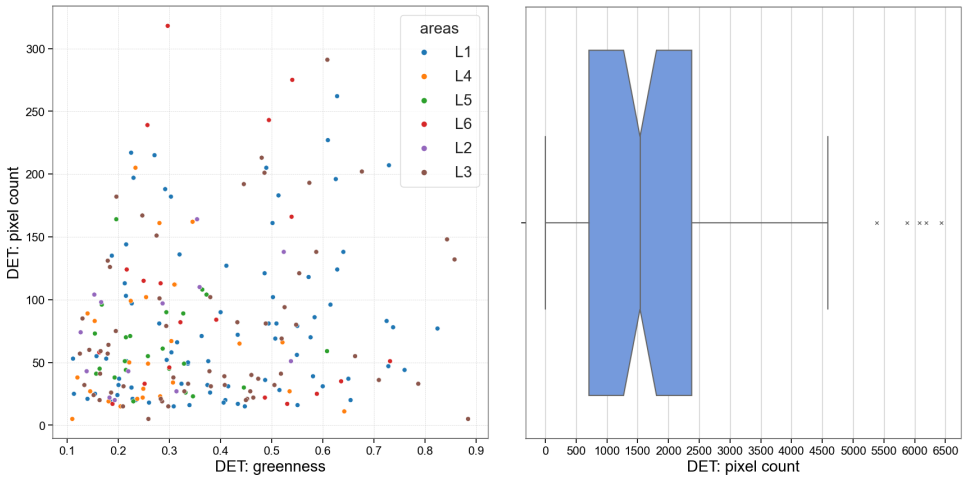


(a) (b)

Figure 4.5: a) Example of how greenness and pixel count may vary within the same RGB-composite. Activity acquisition date 09/12/2019 05:11, Lyngen. The estimated avalanche release date was 06/12/2019 05:11. b) Boxplot with the distribution of DET pixel count in the mean zonal greenness dataset.

# CHAPTER 5

# Results

## 5.1 High-influential data points

As explained in the previous chapter, data points with a detection area consisting of less than 751.5 pixels have been removed to avoid biases in the analysis. This way, we ensure that all data points in the analysis consist of a minimum detected area, in favour of comparing means. Figure 5.1 shows how the excluded and included data points are distributed among potentially true and false data points in the four zones. An example of which data points are removed for mean greenness in AT and DET is seen in Figure 5.2.

## 5.2 Zonal greenness analysis

After the cutoff, the analysis consists of N=67 data points, where 26 are potentially true and 41 are potentially false (Table 5, 6). Each data point represents the mean greenness of a particular zone in a specific area. The mean greenness indicates the relative change in backscatter from a RGB-composite, where 1 indicates the maximum increase and -1 indicates the maximum decrease in relative backscatter change. Described statistics from the zonal greenness analysis are displayed in Table 5.1. The count depends on the number of pixels containing a data value in the greenness raster. The sum is the total of data values from the greenness raster. The mean greenness value is then calculated as the sum divided by the count (Section 4.3). In the following sections, an analysis of the 67 data points are seen.

### 5.2.1 Mean greenness in zones

Figure 5.3 shows the KDE distribution of mean greenness among the four zones. The result shows an increase in mean greenness from NONE to AT and from AT and B40 to DET. DET and B40 have wider distributions resulting in smaller peaks.

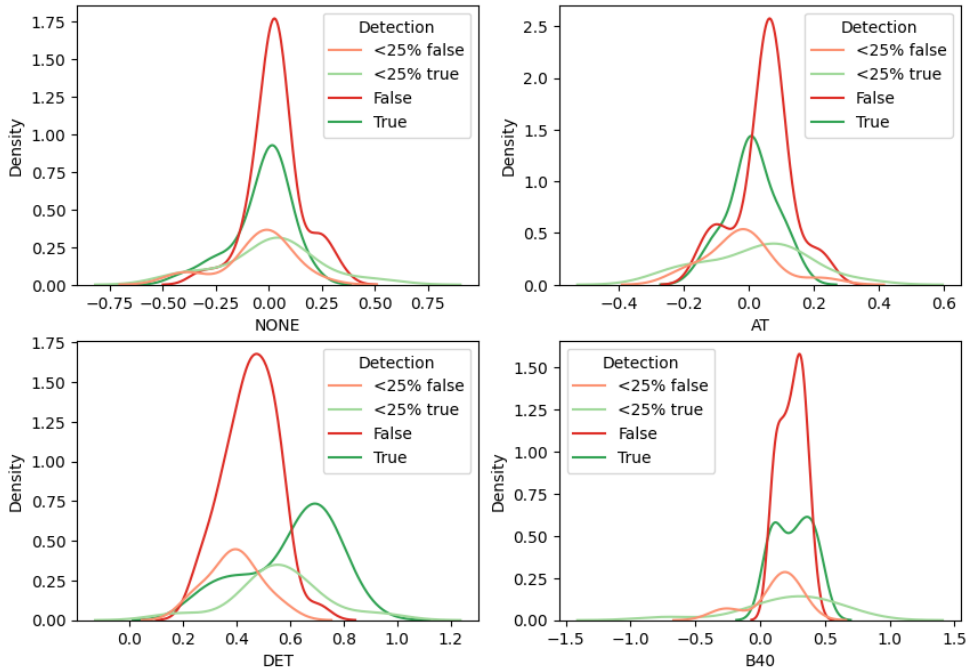


Figure 5.1: Distribution of excluded and included potentially true and false data points. The <25% data points are removed in the following analysis.

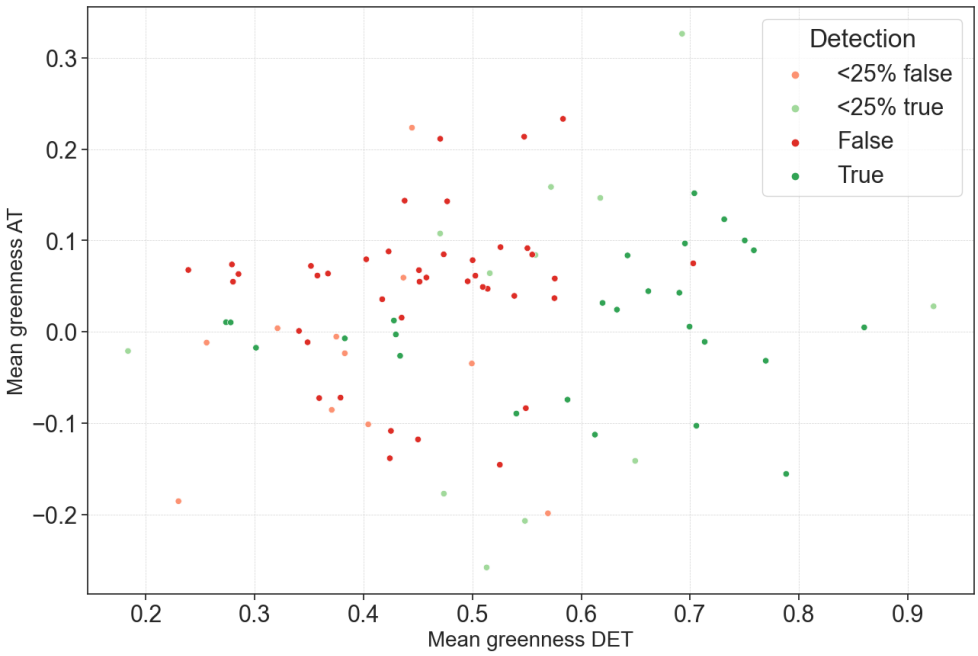


Figure 5.2: Illustration of included and removed data points in a plot for mean greenness in AT and mean greenness in DET.

Table 5.1: Statistics from the zonal greenness analysis, N=67. The table includes statistics on the count, the sum and the mean greenness in the four distinct zones. A similar table with statistics when including high influential data points is seen in the Appendix (Table A7).

| | **NONE** | | | **AT** | | |
|---|---|---|---|---|---|---|
| | count | sum | GI | count | sum | GI |
| no. obs | 67 | 67 | 67 | 67 | 67 | 67 |
| mean | 90416.12 | 813.41 | 0.0084 | 319879.39 | 9518.35 | 0.0314 |
| std | 56974.16 | 13716.59 | 0.1307 | 104806.10 | 28031.55 | 0.0837 |
| min | 35517.00 | -60895.73 | -0.4095 | 126017.00 | -56919.70 | -0.1557 |
| 25% | 54755.00 | -2694.50 | -0.0352 | 250365.94 | -2683.00 | -0.0091 |
| 50% | 81207.00 | 1248.98 | 0.0216 | 281995.86 | 13309.11 | 0.0471 |
| 75% | 101904.00 | 4995.05 | 0.0591 | 400974.93 | 23617.45 | 0.0789 |
| max | 256975.00 | 41936.52 | 0.3339 | 543593.85 | 118900.23 | 0.2332 |

| | **DET** | | | **B40** | | |
|---|---|---|---|---|---|---|
| | count | sum | GI | count | sum | GI |
| no. obs | 67 | 67 | 67 | 67 | 67 | 67 |
| mean | 2378.03 | 1223.93 | 0.5108 | 2957.46 | 689.21 | 0.2491 |
| std | 1327.30 | 816.35 | 0.1484 | 1728.77 | 447.65 | 0.1161 |
| min | 783.00 | 298.44 | 0.2390 | 929.00 | 52.22 | 0.0405 |
| 25% | 1455.50 | 695.65 | 0.4201 | 1760.00 | 353.20 | 0.1346 |
| 50% | 2020.00 | 1013.45 | 0.5002 | 2311.00 | 612.45 | 0.2634 |
| 75% | 2901.00 | 1461.53 | 0.6161 | 3666.00 | 902.32 | 0.3324 |
| max | 6429.00 | 4673.68 | 0.8601 | 8549.00 | 2311.40 | 0.4752 |

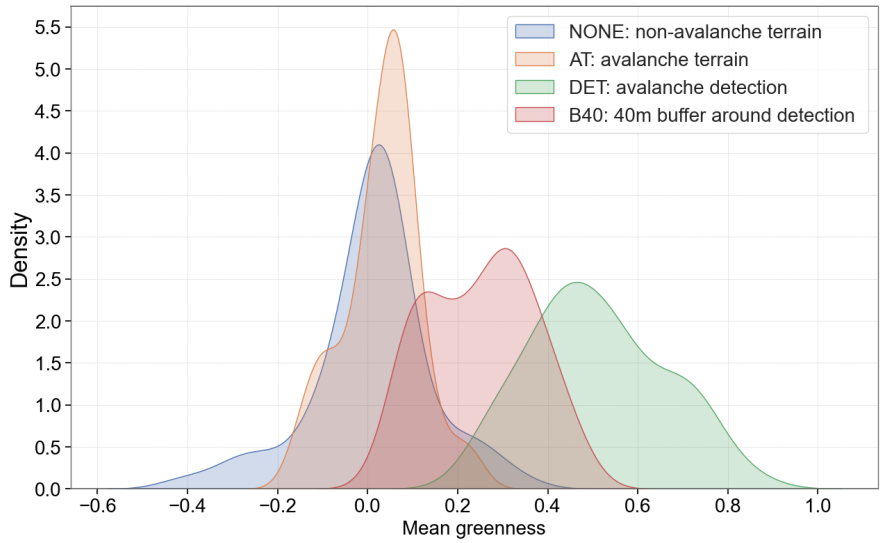


Figure 5.3: KDE-plot visualising the distribution of mean greenness in the four zones. An increase is seen from NONE to AT, B40 and DET. DET has a small overlap with NONE and AT, compared with B40.

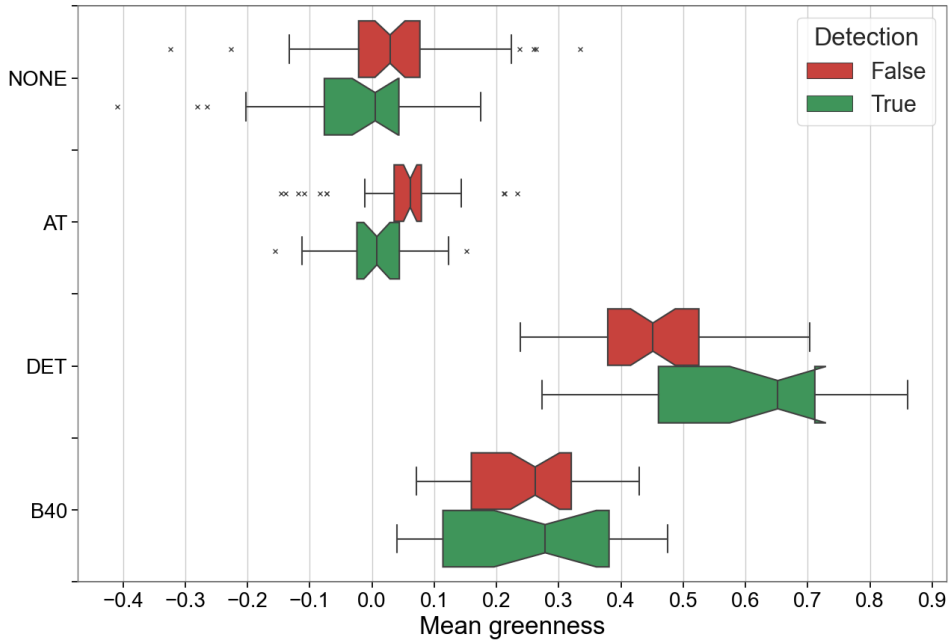


Figure 5.4: Distributions of the mean greenness in the four zones visualised in boxplots, separated between potentially true and false detections. Medians are shown with lines inside each box. The lower and upper quartiles are shown as each box border. The upper and lower whisker displays the interquartile range.

The distribution of mean greenness in the zones with separation between potential true and false detections is visualised in Figure 5.4. Potentially false detections have a higher mean greenness in NONE and AT than potentially true and lower mean greenness in DET and B40. Both NONE and AT are affected by outliers, more noticeable for false detections. The lowest range is seen in AT. The widest ranges are seen in DET and B40. A wider IQR is seen for potentially true detections in DET and B40. The notch, describing the 95% confidence interval for the median, is significantly wider for potentially true detections in all four zones.

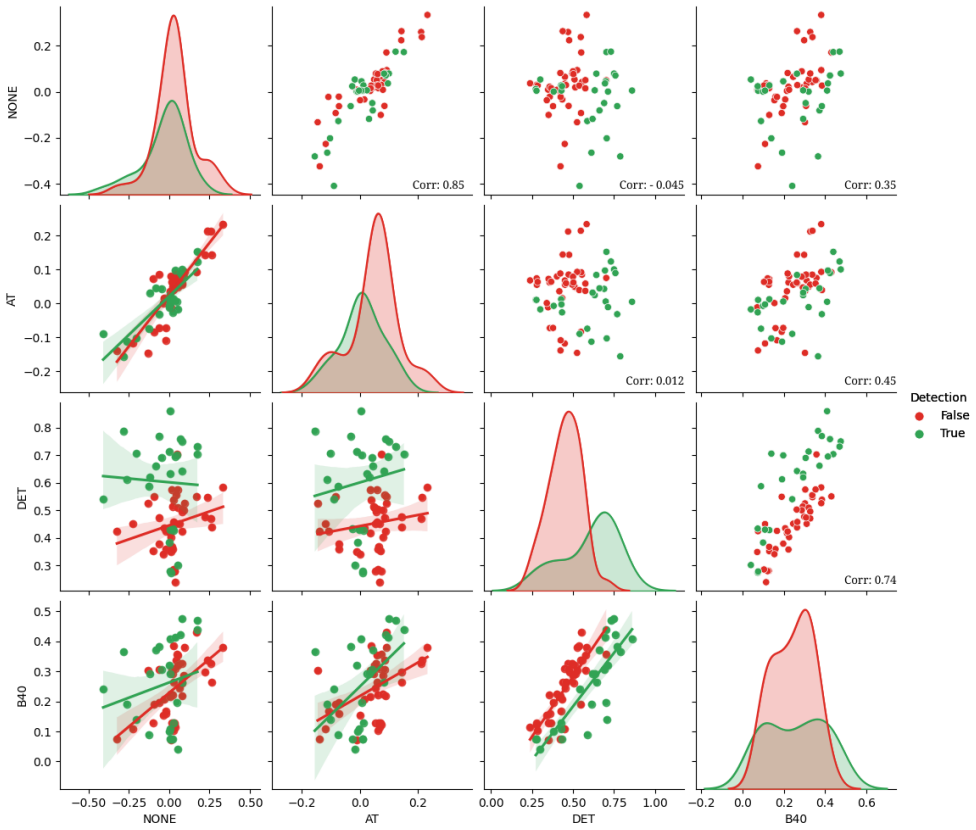


Figure 5.5: Three-parted pair plot of mean greenness values in zones. Upper diagonal shows scatterplots of data and belonging correlation. On the diagonal, a KDE-plot shows the distribution between true and false. The lower diagonal shows a linear regression model for subcategories true and false. The shadowed area shows a 95% confidence interval for the LRM, created by bootstrapping.

The upper diagonal in Figure 5.5 shows a strong correlation between mean greenness in NONE vs AT (0.85) and DET vs B40 (0.74). The lower diagonal shows a similar trend for true and false detections for NONE vs AT. Similar trends are also seen in DET vs B40. However, a more "layered" linear regression

model is displayed. The mean greenness in DET has low correlation with NONE and AT. The related linear regression model shows an inverse trend for DET vs NONE; potentially false detections show a positive trend, whereas the potentially true detections present a slightly negative trend. The linear regression model for DET vs AT illustrates a severe layered trend between potentially true and false detections. Moderate correlation is seen in B40 vs AT and B40 vs NONE, both with positive trends.

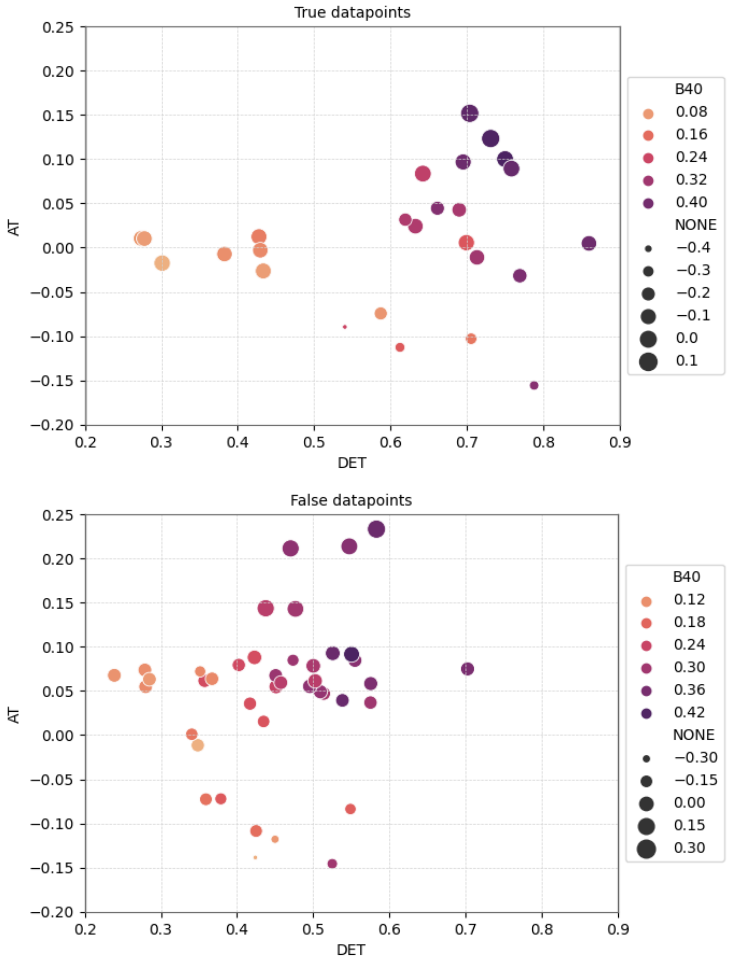


Figure 5.6: 4-dim plot showing the relationship between zonal mean greenness. The y-axis illustrates greenness in avalanche terrain. The x-axis shows greenness in the detection area. Greenness in non-avalanche terrain is displayed as point size. Greenness in the buffer area is shown as colour intensity. Plotted separately for true (top) and false (bottom) data points.

The relationship between mean greenness in all four zones, plotted separately for true and false data points, are seen in Figure 5.6. The colour intensity tends to increase in the x-direction, while point size increases in the y-direction

for both true and false data points. Thus, greenness in NONE increases with increasing mean greenness in AT, and greenness in B40 increases with increased greenness in DET. This is related to the correlation between the above-mentioned zones, seen in Figure 5.5. True data points have a higher DET greenness than false data points. Except for the seven data points with low greenness in B40, true data points generally have a mean greenness in the detection area above 0.53. False data points generally have lower mean greenness than 0.6. False data points also have higher greenness in NONE and AT than true data points.

### 5.2.2 Zonal contrasts

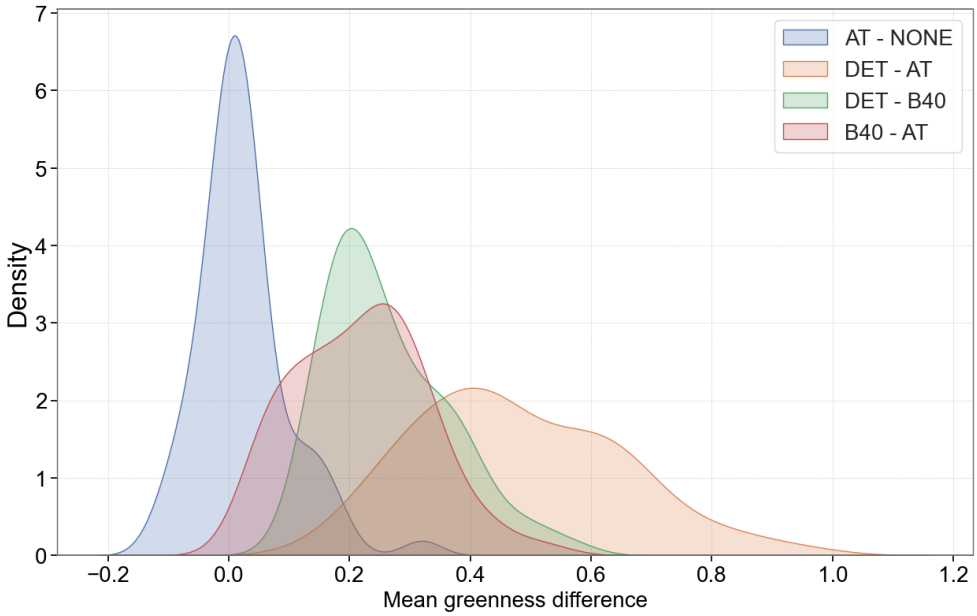


Figure 5.7: KDE-plot visualizing the distributions of the mean greenness contrasts from non-avalanche terrain to avalanche terrain (AT - NONE), avalanche terrain to the detected area (DET - AT), buffer area to detected area (DET - B40), and avalanche terrain to buffer area (B40 - AT).

In the following section, mean greenness contrasts between the zones have been analysed. Figure 5.7 illustrates the distributions of the mean greenness contrasts between zones. The lowest greenness contrast is between NONE and AT, with a peak slightly above zero. The distribution is also the most narrow. Further, a left-skewed peak at $\approx 0.2$ is seen for the mean greenness contrast between B40 to DET, along with a broader distribution. The mean greenness contrast between AT and B40 has a right-skewed peak at $\approx 0.26$ and an even wider distribution. The widest distribution is seen in the mean greenness contrast between AT and DET, with a peak $\approx 0.4$.

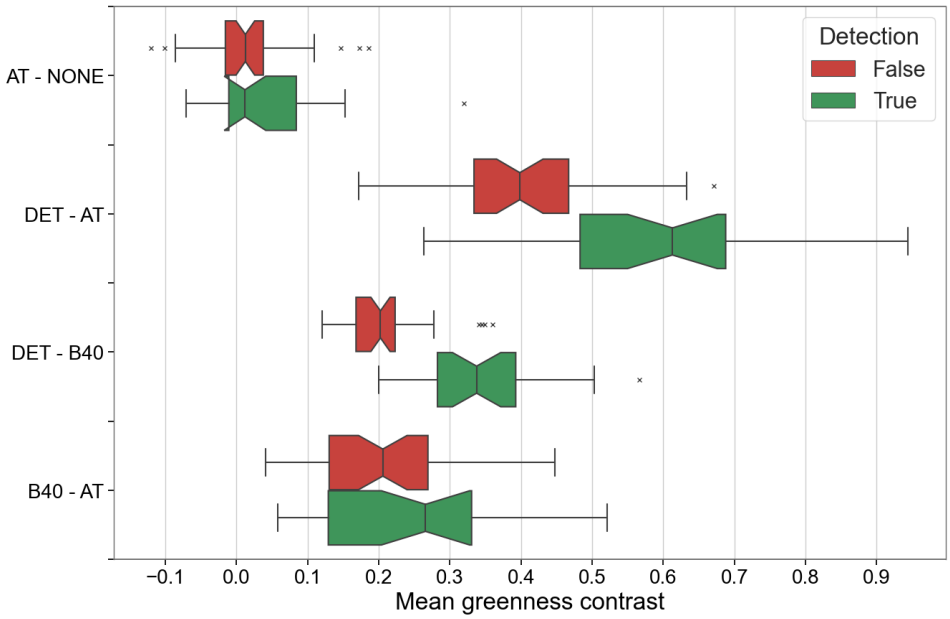


Figure 5.8: Distributions of the mean greenness contrasts visualised in boxplots, separated between potentially true and false detections. Medians are shown with lines inside each box, with a 95% C.I. illustrated by the notch. The lower and upper quartiles are shown as each box border, resulting in the interquartile range (IQR). The lower and upper whisker illustrates the minimum and maximum. The figure illustrates the contrasts between zones.

Figure 5.8 shows separate distributions of zonal contrasts for potentially true and false detections. The median mean greenness contrast is remarkably higher for potentially true detections in all zonal contrasts except AT-NONE. Both contrasts in DET-AT and DET-B40 show a good separation between potentially true and false detections. A contrast of 0.48 or higher between the detected area and the avalanche terrain excludes 78% of the potentially false detections while including 73% of the true detections. Similarly, a contrast of 0.25 between the buffer area and the detected area excludes 83% of the potentially false detections and includes 92% of the true detections. 73% of the potentially true data points had a contrast above 0.48 in DET-AT and 0.25 in DET-B40, while 76% of the potentially false data points had a contrast of less than 0.48 in DET-AT and 0.25 in DET-B40.

The upper diagonal in Figure 5.9 shows that the contrast AT-NONE correlates the lowest with the three other zonal contrasts. The related linear regression models on the lower diagonal show layered, positive trends with increased DET-AT and DET-B40. When plotted against B40-AT, the potentially false detections have a strong negative trend. The highest correlations are seen in DET-AT vs DET-B40 and DET-AT vs B40-AT, with equally strong, positive

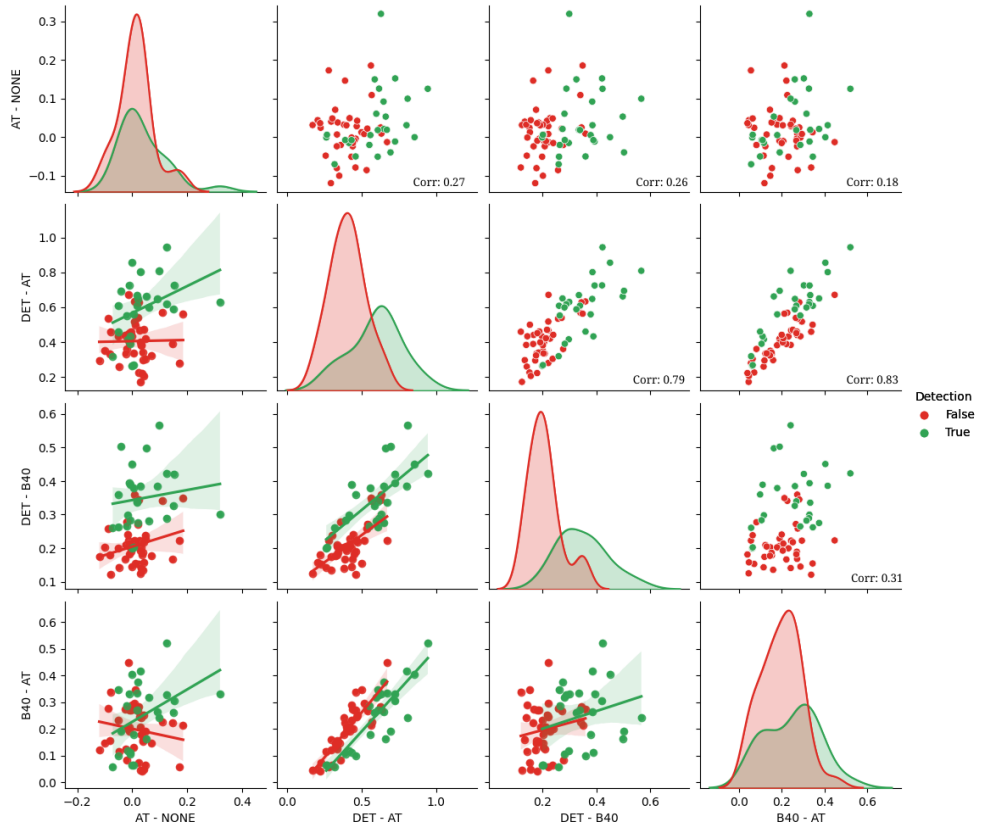


Figure 5.9: Three-parted pair plot of mean greenness contrasts between zones. Upper diagonal shows a scatterplot of data and belonging correlation. A KDE plot shows the distribution between true and false on the diagonal. The lower diagonal shows a linear regression model for subcategories true and false. The shadowed area shows a 95% confidence interval for the LRM, created by bootstrapping.

trends in the related linear regression models on the lower diagonal. B40-AT vs DET-B40 has a weak correlation. DET-AT vs DET-B40 and B40-AT vs DET-B40 show good separation between true and false datapoints on the diagonal.

Figure 5.10 indicates a strong relationship between greenness in DET against greenness contrasts in DET-AT, DET-B40 and B40-AT. DET vs DET-B40 and B40 vs DET-B40 show good separation between potentially true and false data points on the diagonal, where B40 vs DET-B40 has the lowest correlation in the figure.

Figure 5.11 demonstrates the relationship between the mean zonal greenness contrasts. The point sizes, i.e., the contrast in NONE-AT, are distributed randomly in the plot. The contrast in AT-DET tends to increase when the

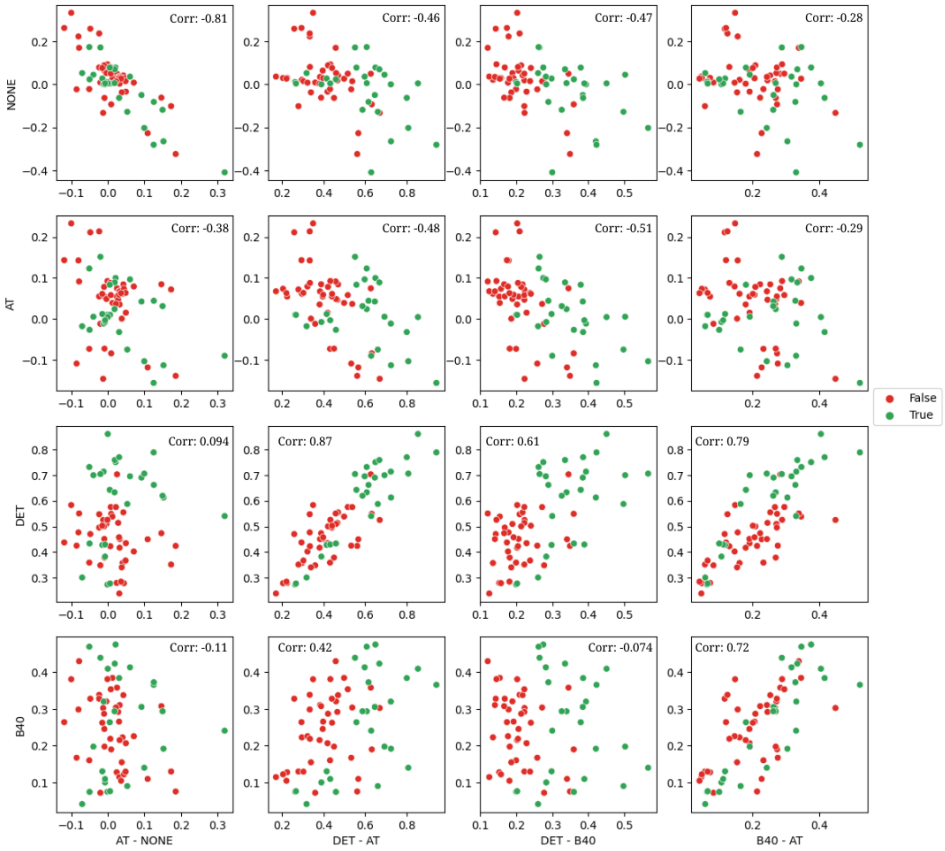


Figure 5.10: Scatterplot between each zonal greenness (y-axis) and the four zonal contrasts (x-axis).

contrast also increases in AT-B40, and B40-DET. True data points generally have a contrast higher than 0.25 in DET-B40. False data points generally have a contrast lower than 0.27.

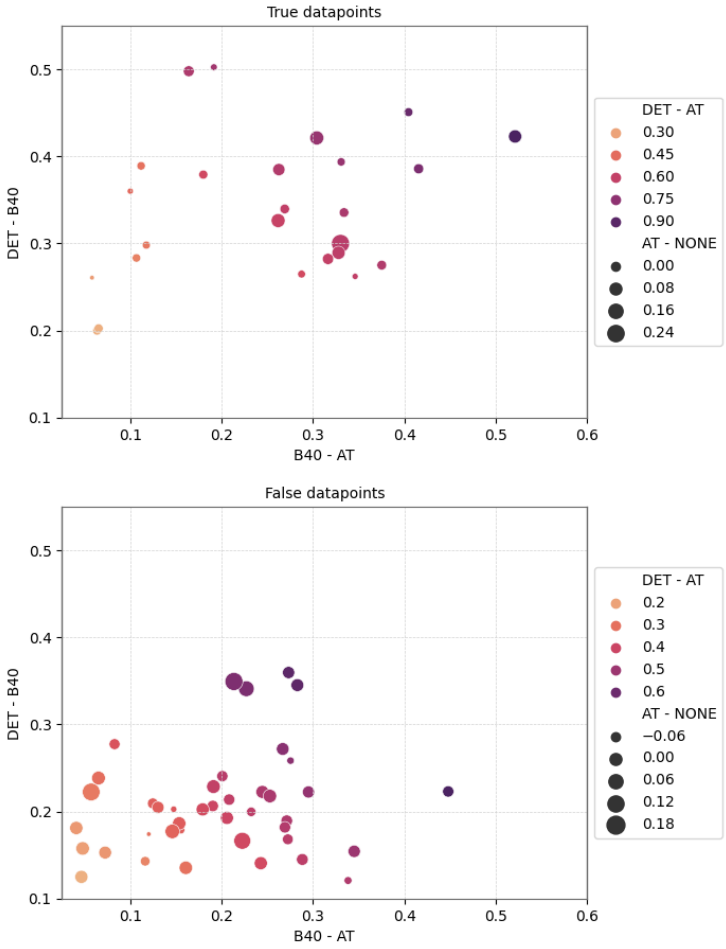


Figure 5.11: 4-dimensional plot showing the relationship between zone contrasts for true data points. The y-axis shows the contrast between the buffer zone and the detection zone. The x-axis shows the contrast between avalanche terrain and the buffer zone. The contrast between avalanche terrain and the detected area is shown in colour intensity. The contrast between non-avalanche terrain and avalanche terrain is shown in point size.

## 5.3 Case study

The preceding section has presented findings indicating that it is possible to distinguish between potentially true and false detections based on the contrast between the buffer area and the detected area, as well as between the avalanche terrain and the detected area (Figure 5.8).

A case study was performed on eight previously unseen RGB composites to assess the influence of varying meteorological conditions between T0 and T1 on zonal greenness contrasts. The aim was to determine if the threshold values from the zonal greenness analysis could be applied to differentiate between potentially true and false detections in further images, based on the observed contrasts.

Weather data were obtained for three different altitudes (lower, middle and higher) in both areas, as explained in Section 3.2.5. Air temperatures were analysed for reference and activity acquisition dates to interpret wet or dry snow conditions. The influence of wind and precipitation was interpreted with qualitative statements. Three change detection images were identified as wet to dry transition (case A) and three others as no transition (case B). All cases were selected from available RGB-composites that matched the qualification criteria for many detections (Section 4.2.1). It should be noted that no cases of dry-wet snow conditions were found. Table 5.2 provides an informative overview of the cases and the meteorological influences.

### Case A: Transition from wet (T0) to dry (T1) snow

Case A1 presents a scenario from area L1, with five detections (Figure 5.12, Table 5.2). The air temperatures decreased from above to below zero for higher altitudes. Stronger winds and precipitation influenced the activity acquisition date. The RGB-composite comprises large, green areas where the relative backscatter has increased. The detections are seen mainly in the SW direction, with low contrast to the surrounding area.

Case A2 is located in R3, with 21 detections (Figure 5.13, Table 5.2). The air temperatures decreased from above to below zero for lower altitudes. Strong winds influenced both the reference and activity acquisition dates. The reference acquisition date was influenced by precipitation. The RGB-composite shows coherent green areas at specific altitudes, best-seen top left around the mountain top. This may be due to the transition of wet to dry snow at the same altitude. The detections are unusually shaped and placed. In lower areas, some reduced backscatter is visible in purple.

Case A3 is located in R3, with 8 detections (Figure 5.14, Table 5.2). The air temperature at the middle altitude transitioned from above to below zero. No wind or precipitation of significance influenced the acquisition dates. The

RGB-composite shows coherent areas of increased backscatter, especially in the S and SE directions. Two of the detections were detected in a relatively purple area.

### Case B: Similar snow conditions in T0 and T1

Case B1 is located in area L1, where 35 detections occurred (Figure 5.15, Table 5.2). The air temperatures were below zero at all altitudes for both acquisition dates. No wind of significance on the acquisition dates. The reference acquisition date was influenced by precipitation. The RGB-composite is relatively green, with little contrast between the detections and the surrounding area.

Case B2 is located in area L1, with 49 detections (Figure 5.16, Table 5.2). The air temperatures were below zero at all altitudes for both acquisition dates. Strong winds and precipitation influenced the reference acquisition date. The RGB-composite is highly affected by reduced backscatter in lower altitudes. Some coherent areas with increased backscatter are seen in higher altitudes and inside valleys. The detections are tongue-shaped and often most in high contrast to the surrounding area with decreased backscatter.

Case B3 is located in R3, with 44 detections (Figure 5.17, Table 5.2). The air temperature in the higher altitudes was below zero at both acquisition dates. Both the reference and activity acquisition dates were under strong influence of wind and precipitation. The RGB-composite shows mainly a reduction or no change in backscatter.

Table 5.2: Acquisition dates and meteorological conditions in reference and activity image in the case studies. The influence of wind and precipitation is interpreted from the last 24 hours before acquisition dates. Wind is defined as moderate (<10 m/s) and strong (>10 m/s). Precipitation is defined as yes or no. Temperatures and the resulting transition are seen for each altitude (higher, middle and lower).

| Case | Date (ref) | Date (act) | Wind (ref) | Wind (act) | Prec. (ref) | Prec. (act) | Altitude [masl.] | T. (ref) [$°C$] | T. (act) [$°C$] | Trans. |
|---|---|---|---|---|---|---|---|---|---|---|
| A1 | 19/05/19 05:09 | 31/05/19 05:11 | moderate | strong | no | yes | 1244 | 5.7 | -2.0 | wet-dry |
| | | | | | | | 671 | 7.7 | 2.6 | wet-wet |
| | | | | | | | 32 | 7.6 | 2.7 | wet-wet |
| A2 | 08/02/20 05:55 | 14/02/20 05:54 | strong | strong | no | yes | 1685 | -1.0 | -9.6 | dry-dry |
| | | | | | | | 687 | 3.0 | -7.7 | wet-dry |
| | | | | | | | 135 | 3.3 | -3.2 | wet-dry |
| A3 | 03/04/19 17:02 | 09/04/19 17:03 | moderate | moderate | no | no | 1685 | -4.5 | -11.2 | dry-dry |
| | | | | | | | 687 | 2.4 | -2.2 | wet-dry |
| | | | | | | | 135 | 5.5 | 3.6 | wet-wet |
| B1 | 24/04/20 05:20 | 30/04/20 05:19 | moderate | moderate | yes | no | 1244 | -7.3 | -10.2 | dry-dry |
| | | | | | | | 671 | -8.3 | -6.4 | dry-dry |
| | | | | | | | 32 | -3.2 | -8.2 | dry-dry |
| B2 | 11/01/19 16:06 | 16/01/19 16:07 | strong | moderate | yes | no | 1244 | -8.7 | -12.5 | dry-dry |
| | | | | | | | 671 | -5.0 | -9.6 | dry-dry |
| | | | | | | | 32 | -4.7 | -9.2 | dry-dry |
| B3 | 09/05/20 05:46 | 15/05/20 05:46 | strong | strong | yes | yes | 1685 | -4.0 | -8.1 | dry-dry |
| | | | | | | | 687 | 0.3 | -1.3 | dry-dry |
| | | | | | | | 135 | 2.3 | -0.2 | wet-wet |

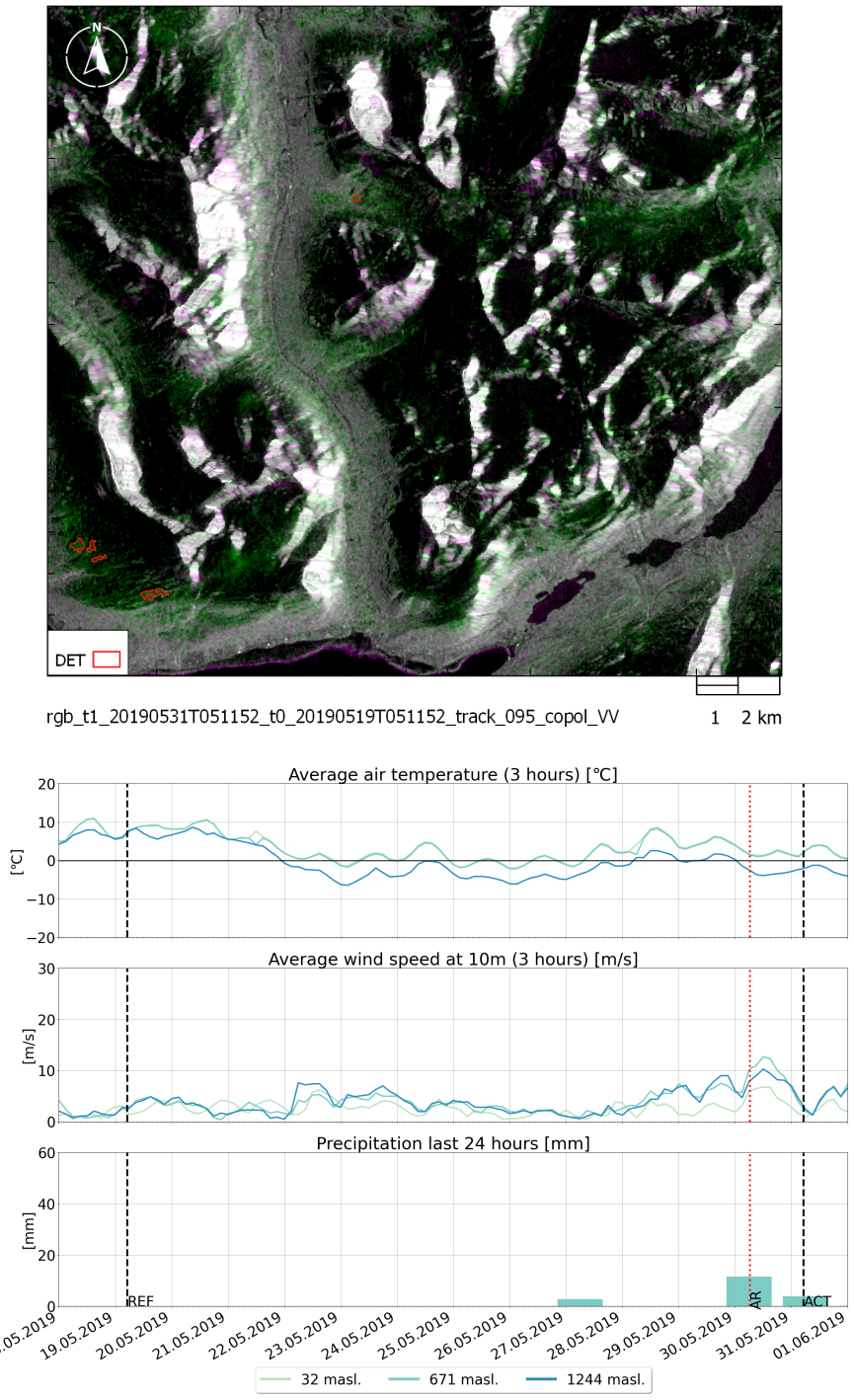


Figure 5.12: Case A1, located in L1, Lyngen. The RGB-composite is composed of two images with a 12-day return period. Detections are shown with red outlines. Avalanche release time is marked with AR. The temperature, wind and precipitation between the acquisition dates are plotted for three altitudes.

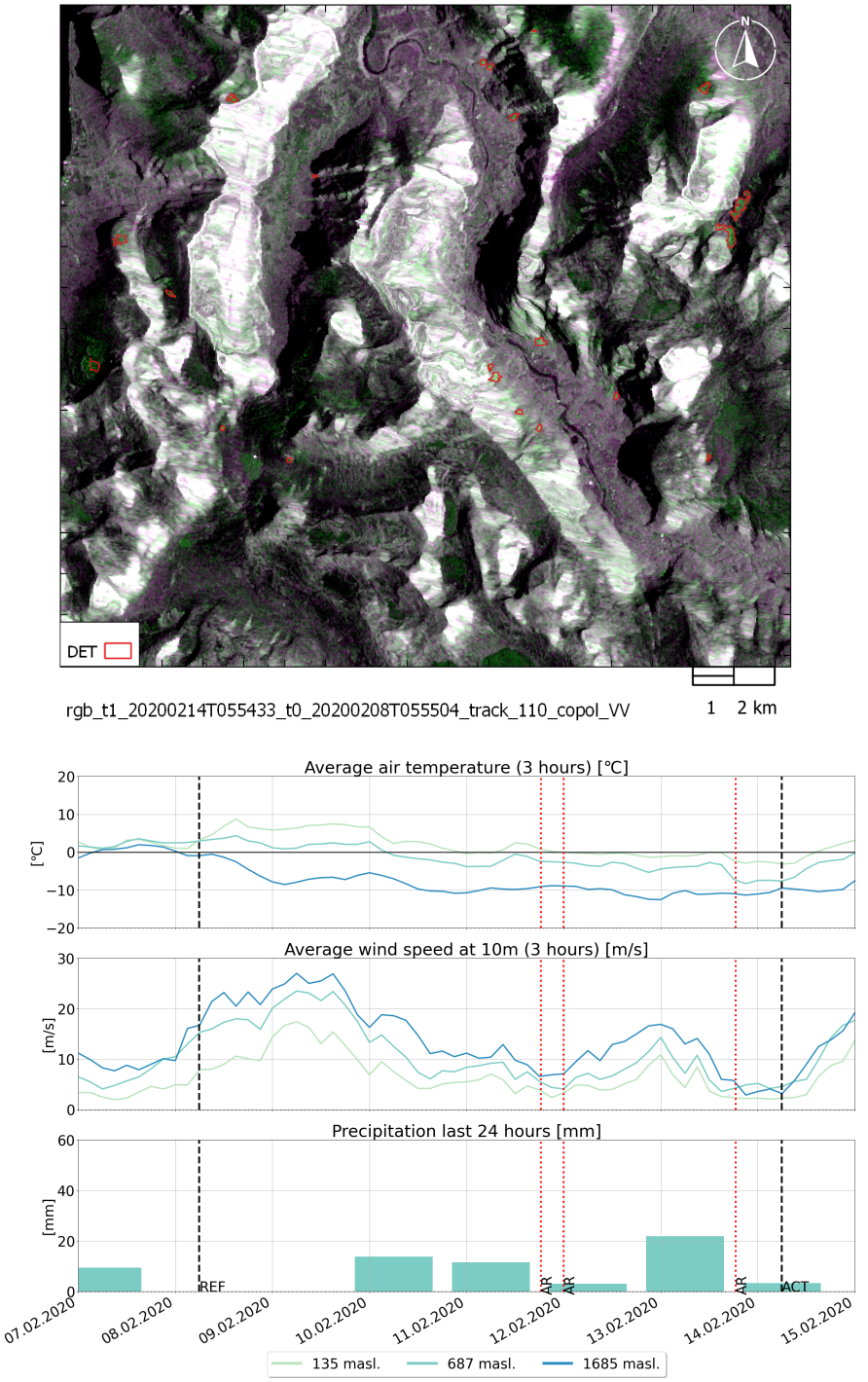


Figure 5.13: Case A2, located in R3, Romsdal. Detections are shown with red outlines. Avalanche release times are marked with AR. The temperature, wind and precipitation between the acquisition dates are plotted for three altitudes.

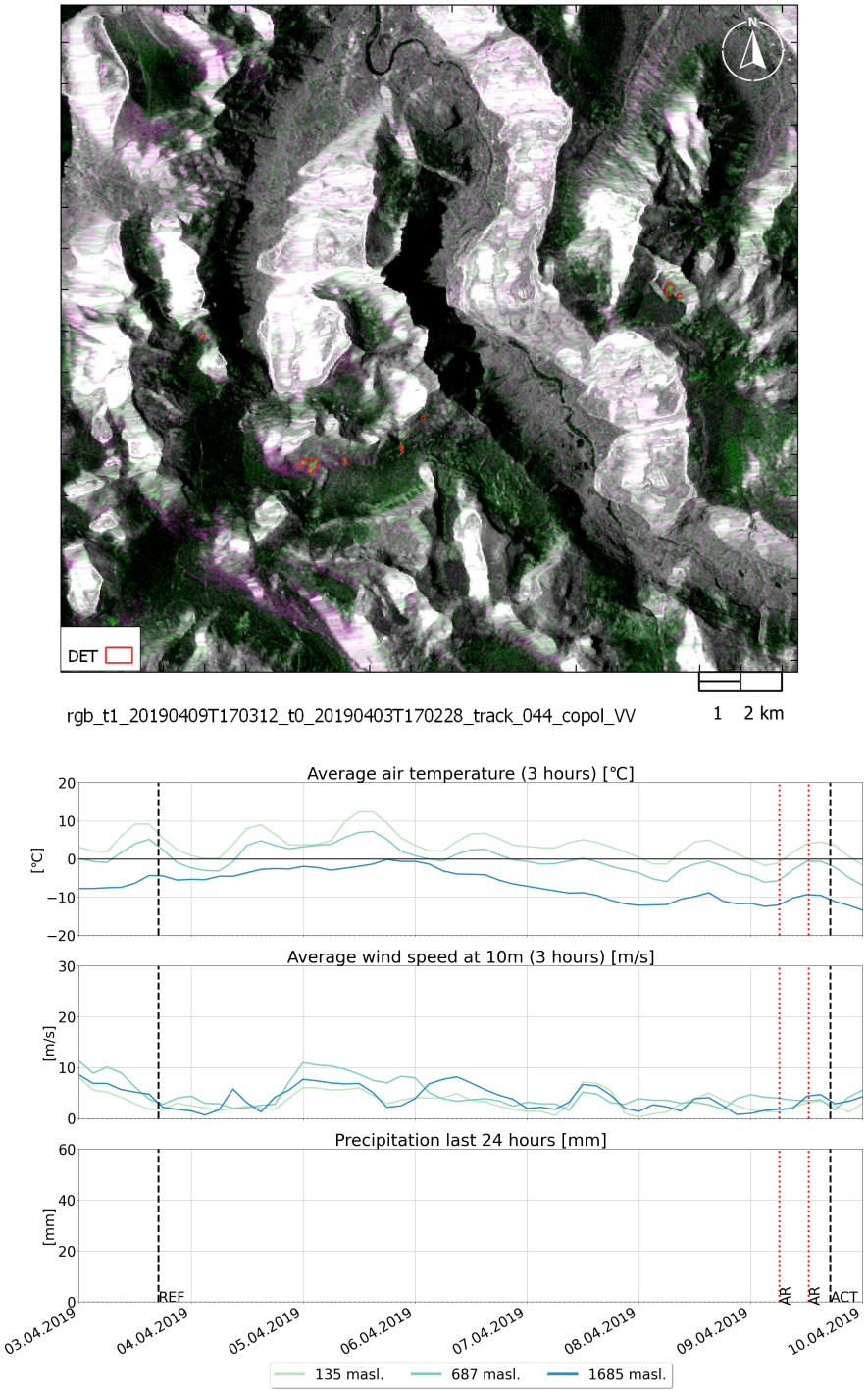


Figure 5.14: Case A3, located in R3, Romsdal. Detections are shown with red outlines. Avalanche release times are marked with AR. The temperature, wind and precipitation between the acquisition dates are plotted for three altitudes.

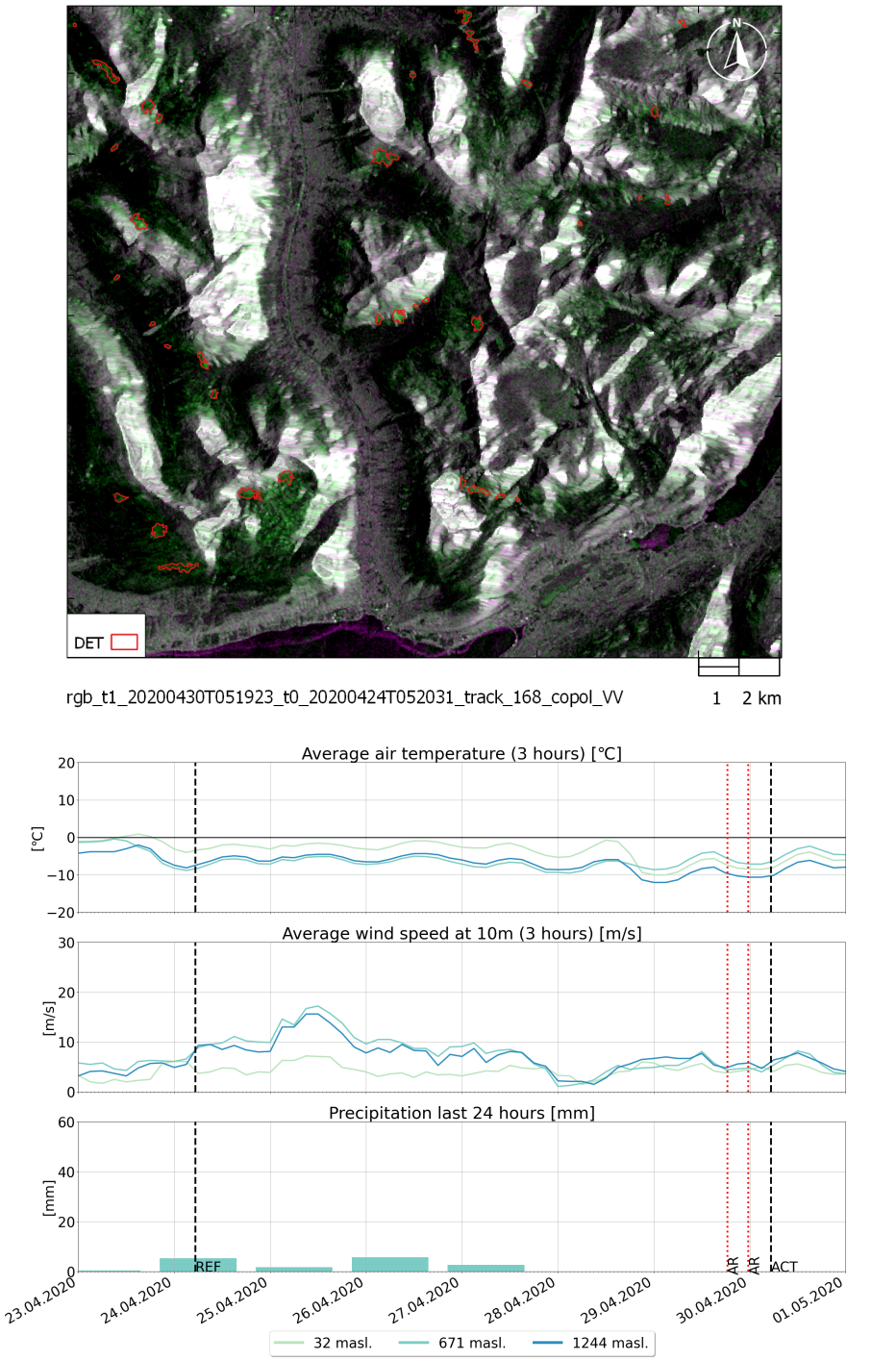


Figure 5.15: Case B1, located in L1, Lyngen. Detections are shown with red outlines. Avalanche release times are marked with AR. The temperature, wind and precipitation between the acquisition dates are plotted for three altitudes.

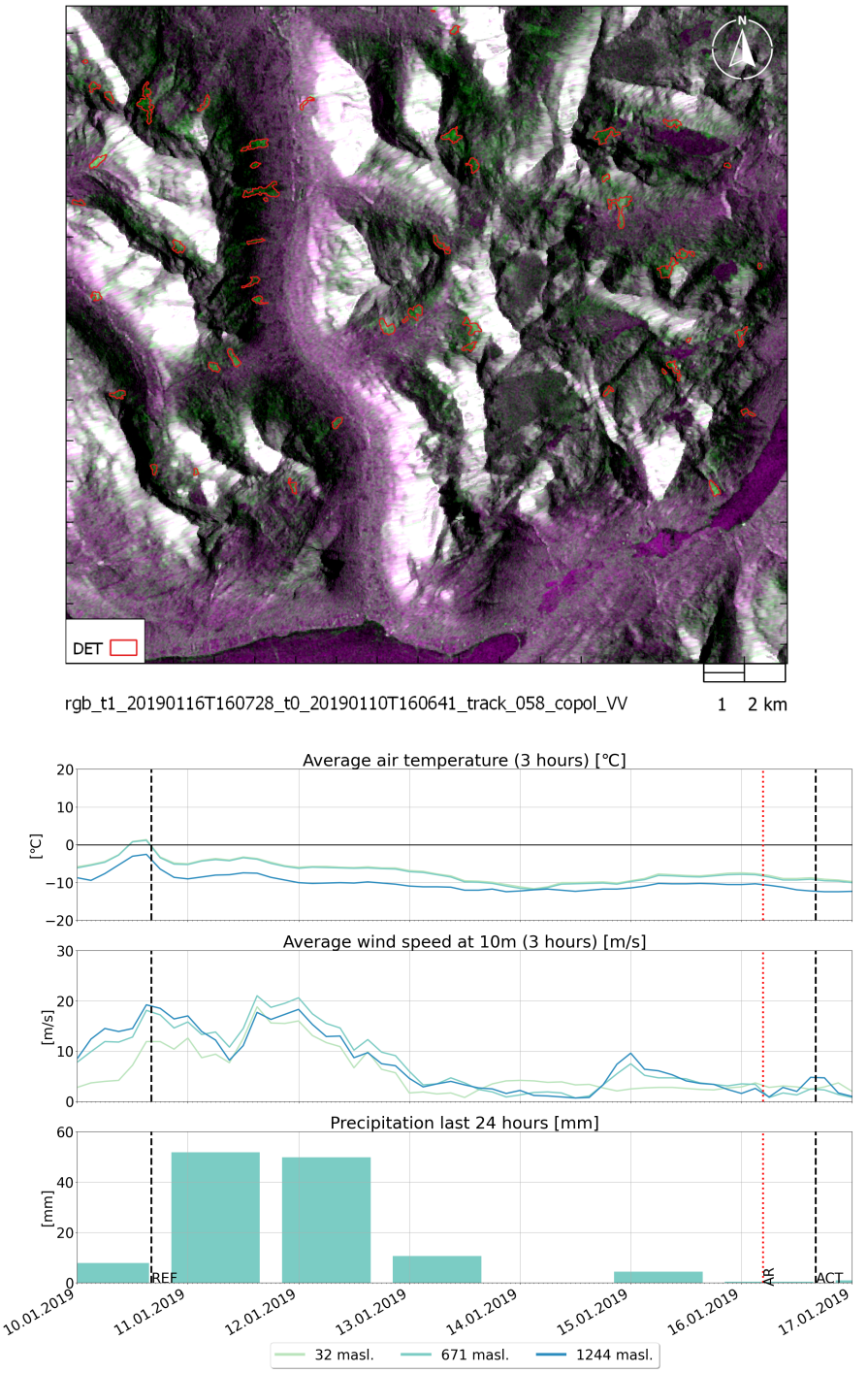


Figure 5.16: Case B2, located in L1, Lyngen. Detections are shown with red outlines. Avalanche release time is marked with AR. The temperature, wind and precipitation between the acquisition dates are plotted for three altitudes.

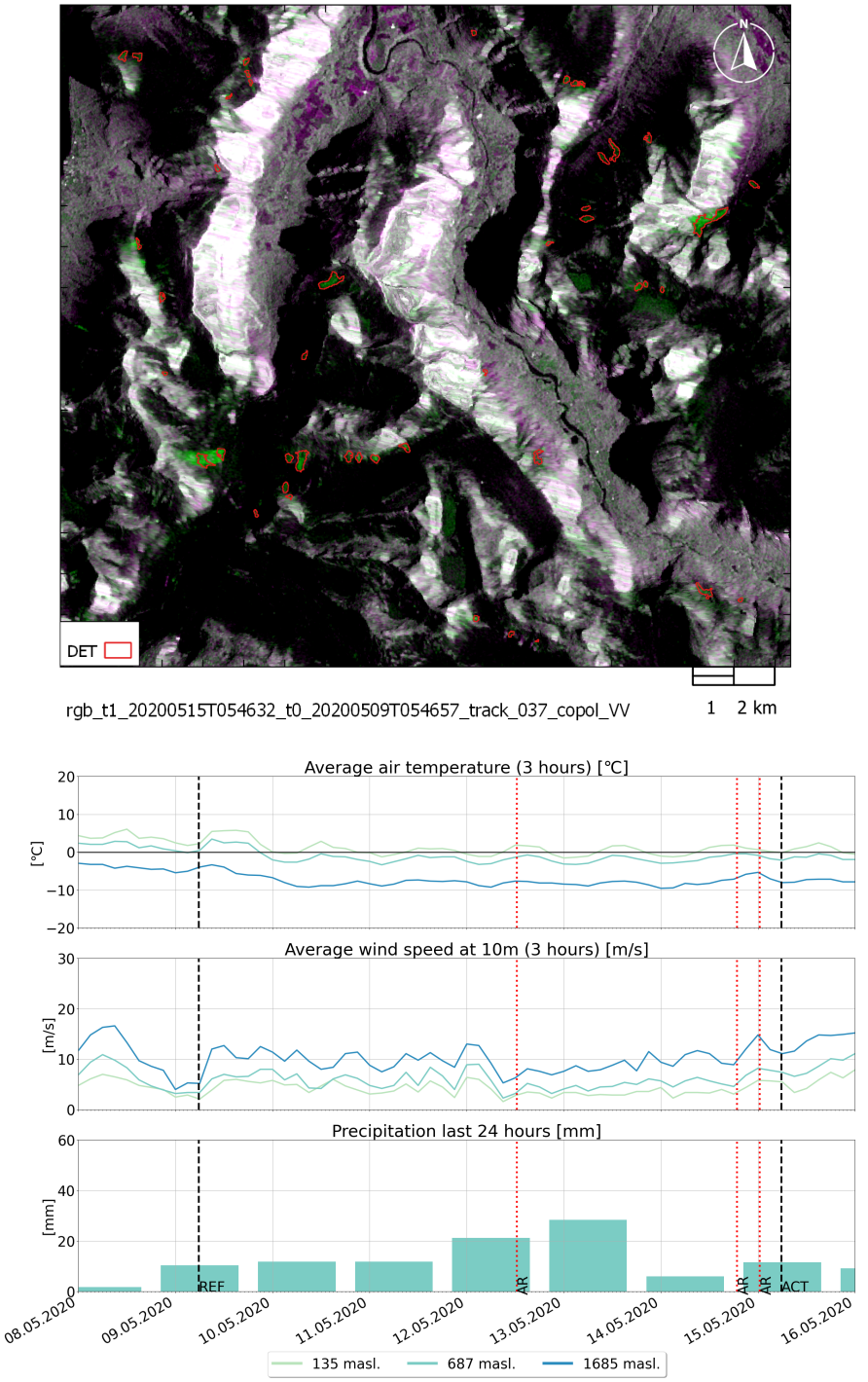


Figure 5.17: Case B3, located in R3, Romsdal. Detections are shown with red outlines. Avalanche release times are marked with AR. The temperature, wind and precipitation between the acquisition dates are plotted for three altitudes.

### 5.3.1 Zonal greenness in cases

The mean zonal greenness values have been calculated for the cases in A and B. The results from each zone and each contrast are shown in Table 5.3. To compare with the separation thresholds of 0.48 (DET-AT) and 0.25 (DET-B40), two plots have been created for our cases showing the DET-B40 and DET-AT contrasts. In the next chapter, each case will be discussed to see if we can determine a RGB-composite as a potentially true or false detection based on the contrasts between DET and B40 or AT.

Table 5.3: Mean greenness values and greenness contrasts from our case studies

| Case | NONE | AT | DET | B40 |
|---|---|---|---|---|
| A1 | 0.2579 | 0.1772 | 0.8888 | 0.7895 |
| A2 | 0.0035 | -0.0262 | 0.2986 | 0.1034 |
| A3 | 0.0986 | 0.1070 | 0.2952 | 0.0775 |
| B1 | 0.0736 | 0.1042 | 0.6295 | 0.4070 |
| B2 | -0.1593 | -0.0470 | 0.4182 | 0.1409 |
| B3 | -0.0752 | -0.0335 | 0.7429 | 0.3498 |
| | AT-NONE | DET-AT | DET-B40 | B40-AT |
| A1 | -0.0807 | 0.7116 | 0.0992 | 0.6123 |
| A2 | -0.0297 | 0.3249 | 0.1952 | 0.1296 |
| A3 | 0.0083 | 0.1882 | 0.2178 | -0.0295 |
| B1 | 0.0306 | 0.5253 | 0.2225 | 0.3028 |
| B2 | 0.1123 | 0.4652 | 0.2773 | 0.1879 |
| B3 | 0.0417 | 0.7765 | 0.3931 | 0.3834 |

Figure 5.18 shows how the contrasts (DET-AT and DET-B40) for case A (wet to dry transition) interact with the threshold results from Section 5.2.2. A1 shows high contrast between the detection zone and avalanche terrain (0.71, Table 5.3), and low contrast between the detection zone and buffer zone (0.10, Table 5.3). The case places itself high above the threshold for DET-AT and below the threshold for DET-B40. The two contradictory contrasts are due to high greenness values in all zones (relative to Figure 5.4). In A2 the contrasts between detections and avalanche terrain (0.32, Table 5.3) and between detections and buffer zone (0.20, Table 5.3) are placed below the two thresholds. The zonal greennesses are not significantly high, especially in DET, resulting in a lack of potential for high contrasts. The same scenario is seen in A3, with the contrast between detections and avalanche terrain (0.19, Table 5.3), and detections and avalanche terrain (0.22, Table 5.3), both below the threshold. Generally, case A has low contrasts in DET-B40, which fits when compared to the potentially false detections.

A similar figure is seen in Figure 5.19, for case B (no transition). B1 has a contrast above the threshold value in DET-AT (0.53, Table 5.3) and below

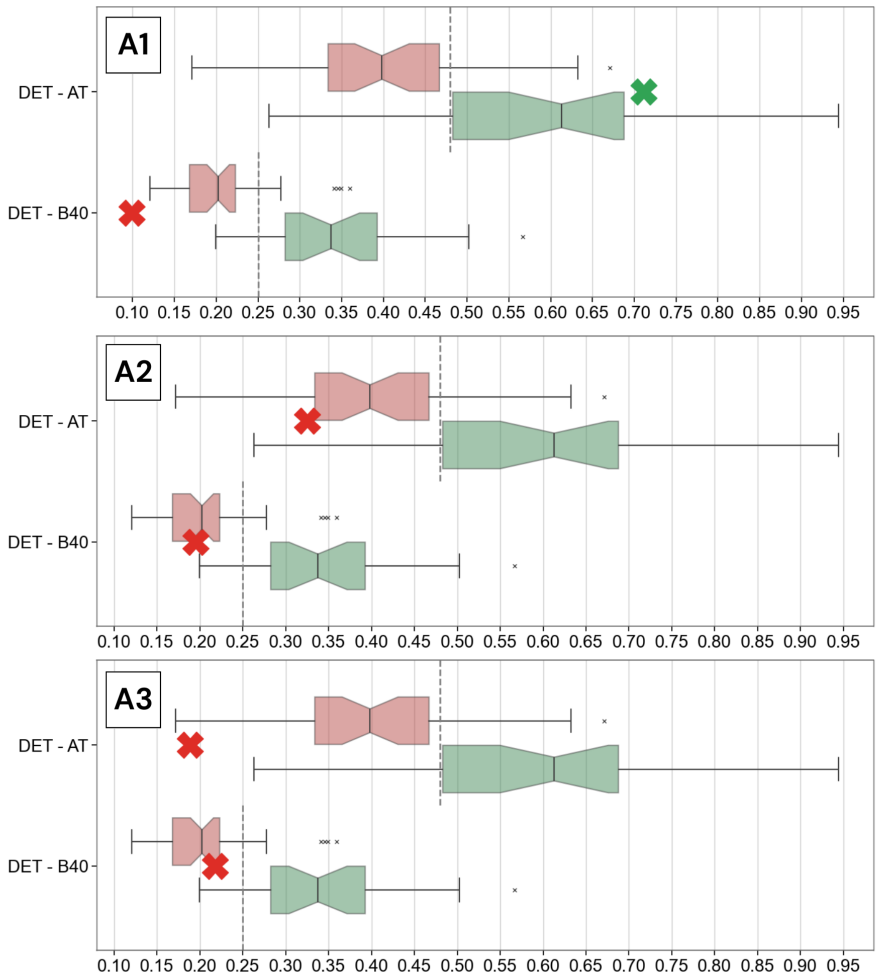


Figure 5.18: The figure illustrates how the mean zonal greenness contrasts from case A are distributed based on the separation value of 0.48 in DET-AT and 0.25 in DET-B40. The separation values are marked with grey dashed lines. The boxplot in Figure 5.8 is reused transparently, with plotted case contrasts as green or red crosses depending on placement relative to the thresholds of true or false. Case A1 has a contrast above 0.48 in DET-AT and below 0.25 in DET-B40. Case A2 and A3 has contrasts below all threshold values.

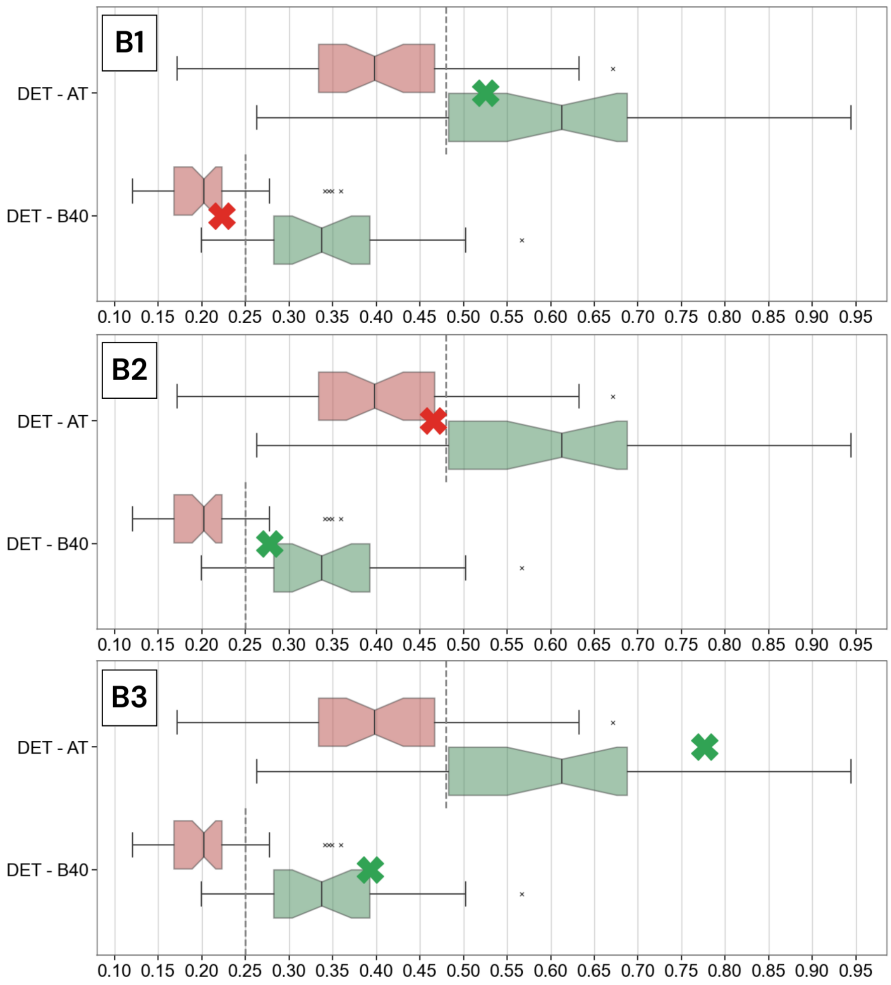


Figure 5.19: The figure illustrates how the mean zonal greenness contrasts from case B are distributed based on the separation value of 0.48 in DET-AT and 0.25 in DET-B40. The separation values are marked with grey dashed lines. The boxplot in Figure 5.8 is reused transparently, with plotted case contrasts as green or red crosses depending on placement relative to the thresholds of true or false. Case B1 has a contrast above 0.48 in DET-AT and below 0.25 in DET-B40. Case B2 has a contrast below 0.48 in DET-AT and above 0.25 in DET-B40. Case B3 has both contrasts above the threshold values.

in DET-B40 (0.22, Table 5.3). As a result of high greenness in the buffer zone (0.41, Table 5.3), the contrast between the detection area to the buffer zone is low. In B2, the contrast between detections and avalanche terrain (0.47, Table 5.3) is slightly below the threshold for DET-AT. The contrast between detections and buffer zone (0.28, Table 5.3) is above the threshold for DET-B40. In this case, a negative greenness is seen in both non-avalanche and avalanche terrain, i.e., a reduction of backscatter. In B3, both contrasts are well above the threshold, with contrasts of 0.78 and 0.39 in DET-AT and DET-B40, respectively (Table 5.3). Here the greenness in the detection zone is high (0.74, Table 5.3).

# CHAPTER 6

# Discussion

In this thesis, we wanted to be able to filter out potentially true and false detections of avalanche debris. By developing a greenness indicator, we were able to quantify the relative backscatter change between a reference and an activity image to a number between -1 and 1. Here 0 indicates no change in backscatter, -1 indicates a maximum decrease in backscatter and 1 indicates a maximum increase. This was used to explain how "green", i.e., how much the backscatter increased, in four defined zones in a total of 12 smaller areas in the avalanche forecasting regions Lyngen and Romsdal: non-avalanche terrain, avalanche terrain, detection polygons and 40 meters buffer zone surrounding each detection polygon. We interpreted the detections as potentially true or false by analysing S1 SAR change detection images combined with weather data and snow observations. This was done to explore if we could use estimates of greenness to separate between potentially true and false detections to improve the detection algorithm. Both mean zonal greenness values and mean zonal greenness differences have been analysed and will, in the following sections, be discussed.

If we expect no detections of avalanche deposits, we would expect similar greenness trends in all four zones. Likewise, we would expect an increase in greenness from non-avalanche terrain to avalanche terrain if we expect the avalanche terrain to contain detections. Further, we would expect an increase from the avalanche terrain to the detection zone, as this area is (mostly) significantly smaller and more concentrated (of greenness) than the avalanche terrain. A 40-meter buffer zone was created around each detection polygon. This was done to investigate the possibility of lower contrasts between the possible avalanche debris and the surrounding, untouched snow for false detections.

We chose to inspect 16 change detection images among images with many detections. All images with many detections, also potentially false detections, have, in one way or another, an increased value of greenness in the detection zone, or else there should not be any false detections in the first place.

## 6.1 Results from zonal greenness analysis

The results in Figure 5.3 show, in favour of our hypothesis, that the greenness increases in the four zones. As expected, a small increase in greenness is seen from NONE to AT, as the AT also contains the detected avalanche debris. Overall, the increase from NONE to AT is small compared to the increase from NONE to DET. This can be explained by AT being many times larger than the size of DET (Table 5.1). The results also show increased greenness from AT to B40 and B40 to DET. An ideal situation would be no increase from AT to B40, as the last mentioned represent a snippet of the AT. This implicates data with elevated greenness in the buffer zone.

The median distribution of mean greenness for potentially false data points in NONE and AT are slightly higher than the potentially true data points (Figure 5.4). Especially AT shows an elevated greenness among potentially false detections, whereas potentially true detections have similar medians in NONE and AT. Theoretically, a transition from wet to dry snow conditions increases relative backscatter (Eckerstorfer and Malnes, 2015; Vickers et al., 2016). This is known as the biggest source of false detections (Eckerstorfer et al., 2019). This can explain the elevated greenness in both NONE and AT for potentially false detections. The potentially true data points have a higher median distribution for DET and B40. Especially DET shows a good separation between potentially true and false data points, where the lower quartile for true overlaps with the median false (Figure 5.4). One surprising, noticeable feature is how potentially true detections have a higher mean greenness in B40 than false.

Figure 5.5 shows how the zonal greennesses are related and how the trends for separated potentially true and false data points are distributed. NONE vs AT and DET vs B40 strongly correlate, indicating zone dependency. When the mean greenness in NONE or DET increases, so does the mean greenness in AT and B40, respectively. The strong, dependent relationship between the zones is also seen in Figure 5.6, where increased mean greenness in NONE is mostly related to increased values in AT and the same for DET and B40. A non-existence relationship exists between AT and DET, and NONE and DET, indicating independence of mean greenness in detections compared to NONE and DET.

Similar figures were made for mean greenness differences to explore the contrasts between the zones (Section 5.2.2). Figure 5.7 implies that the smallest contrast is seen between non-avalanche terrain and avalanche terrain. The widest distribution and highest contrast are seen from AT to DET. This can be explained by the high values of mean greenness in DET compared to AT, as seen in Figure 5.4. Figure 5.8 shows how the zonal differences are distributed among potentially true and false detections. DET-AT and DET-B40 show great

separation between the potentially true and false detections. The previous high mean greenness in B40 for true detections is neglected due to the high greenness in DET, resulting in a separation between true and false where the lower quartile for true overlaps with the upper whisker for false. Furthermore, the median greenness difference between AT and B40 is higher for false than true.

The increase from NONE to AT has a weak correlation to the three other zonal greenness differences (Figure 5.9). An explanation for this can be the layered and different trends for true and false, seen in the linear regression models. The two highest correlated differences can be seen for DET-AT vs DET-B40 and DET-AT vs B40-AT. An explanation for this dependence may be the high correlation between DET and B40 (Figure 5.5).

Similarly, DET-B40 and B40-AT have a weak correlation but separate the potentially true and false data points (Figure 5.9). This figure shows that an increase in B40-AT mainly includes false data points. The potentially true data points are first included when DET-B40 is above 0.2. The relationship between B40-AT and DET-B40 is further explored in Figure 5.10. Here we can see that B40 has a non-existing correlation to DET-B40. This shows independence between variables and good separation between the potentially true and false data points. The weak correlations between AT-NONE and other zonal differences are again seen in Figure 5.11 where the point size is randomly distributed compared to the colour intensity, indicating a strong relationship between DET-AT and B40-AT and DET-B40.

The good separations between potentially true and false detections in DET-AT and DET-B40 are one of the most important findings in this study (Figure 5.8). This result indicates that a threshold could be introduced in the detection algorithm to filter out potentially falsely detected avalanches. The thresholds were drawn in the gap between the potentially true and false detection boxes. A threshold of 0.48 between the detected area and the avalanche terrain excluded 78% of the potentially false detections in our dataset while including 73% of the potentially true detections. Similarly, a threshold of 0.25 between the buffer area and the detected area excluded 83% of the potentially false detections while including 92% of the potentially true detections. It was found that 73% of the potentially true data points had contrasts above 0.48 in DET-AT and 0.25 in DET-B40, while 76% of the potentially false data points had contrasts of less than 0.48 in DET-AT and 0.25 in DET-B40. The threshold was further studied and tested on six previously unseen RGB-change detection images. This will be discussed in the next section in combination with changing meteorological conditions between the acquisition dates.

## 6.2 Evaluation of threshold values

A threshold of 0.48 and 0.25 managed to exclude 78% and 83% of the potentially false detections in DET-AT and DET-B40, respectively. We wanted to test the thresholds for the potential of accepting an unseen change detection image as a potentially true detection. By defining two cases, case A and case B, we were able to explore the thresholds on scenarios with changing meteorological conditions. Case A consisted of three RGB-composites exhibiting a transition from wet to dry snow surface between the two acquisition dates. Similarly, case B consisted of three RGB-composites with similar snow conditions on both acquisition dates. Our results show that if we only considered the threshold between DET-AT as a criterion for a potentially true detection, A1, B1, and B3 would be accepted as true detections. Likewise, if we only considered the threshold between DET-B40 as a criterion for true declaration, B2 and B3 would be accepted as true detections. If we considered both thresholds a criterion, solely B3 would be declared a true detection (Figure 5.18, 5.19).

Interpretation of weather plots and each RGB-composite were conducted to validate our results. All scenarios in case A showed more or less coherent, green areas with the detected polygons in low contrast to the surrounding terrain. A1 had extremely high greenness in all zones and was also our case with the highest air temperature change between the acquisition dates (Figure 5.12, Table 5.3). A2 and A3 had similar greenness values in the detection area (Figure 5.13, 5.14, Table 5.3). All the scenarios in A are suggested to be false detections due to transitioning from wet to dry snow. B1 showed similarities with A1 and is interpreted as false based on the greenness values in the RGB-composite (Figure 5.15, Table 5.3). B2 exhibited two days with heavy snowfall and strong wind, favourable for avalanche release (Figure 5.16). The detections were also in clear contrast to the surrounding area, which was also seen in case B3 (Figure 5.17, Table 5.3). Both B2 and B3 are interpreted as true detections.

Case B2 and B3 are the only cases with contrasts above the threshold values in DET-B40 and are interpreted as the only potentially true detections. The high contrasts in DET-AT for A1 and B1 indicate sensibility to the chosen threshold, especially for RGB-composites with elevated greenness values in all zones. As these are interpreted as potentially false detections, cautiousness must be provided if declaring an image based on only this threshold.

## 6.3 Influence of changing meteorological conditions on greenness

Dry snow exhibits a higher backscatter coefficient than wet snow (Eckerstorfer and Malnes, 2015). As a result, a RGB-composite composed of images where the snow conditions have transitioned from wet to dry between the acquisition

dates, are likely to exhibit elevated greenness values in all zones. This scenario was best seen in the case of A3, with no influence of wind or precipitation, and had high greenness values in all zones (Table 5.3). A similar scenario with wet-to-dry transition and increased greenness in all zones was seen in the case of A1, although with some precipitation the two days before the activity acquisition date (Table 5.3). The results from A1 and A3 are consistent with Eckerstorfer and Malnes (2015). However, case A2 showed decreased greenness in AT and a modest increase in NONE (Table 5.3). One explanation for this could be a reducing effect from the precipitation event two days before the activity acquisition date. However, it is hard to establish if the precipitation was rain or snow due to shifting air temperatures these days.

In the case of B1, we saw an increase of greenness in NONE and AT, similar to A3, but the weather conditions are different (Figure 5.15). First, the air temperatures were stable, below the freezing point. Nevertheless, an increase in greenness was seen. This could be explained by the small precipitation event the day before and on the day of reference acquisition; if in the form of snow, this could have smoothed the surface, resulting in a relative increase in backscatter at the activity acquisition date. B2 and B3 show backscatter reductions in NONE and AT (Table 5.3). This phenomenon is related to the dry-to-wet transition (Vickers et al., 2016). In these cases, we do not have such a transition. From our observations in B2, a large amount of new snow is seen at the reference acquisition date and the day after. Similarly, B3 has small precipitation events throughout the period between acquisition dates. Depending on when, relative to the time of acquisition, a large amount of new snow in combination with strong winds can smooth the surface roughness. This influence was also seen in Antonova et al., (2016), where a study on TerraSAR X-band backscatter values decreased due to a snow event.

### 6.3.1 Differences in greenness due to acquisition conditions

Each RGB-composite comprises two SAR images with similar tracks and geometries, with a 6- or 12 days revisit frequency. A change detection image composed of two images with a 12-days interval may be subject to larger changes in snow properties that affect the greenness values compared to a 6-days interval image. This could explain the highly elevated mean greenness values in all zones in case A1 (Table 5.3). Compared to the other cases, case A1 is the only case with a 12-days acquisition interval. Throughout the 12 days, the area was under the influence of several days of melting and nights of freezing, which could result in a rough, crusty surface with the potential of increased backscatter values in the activity image.

The temporal change detection method detects possible areas of avalanche deposits where increased backscatter has occurred between the acquisition dates. As explained earlier, each detection has an estimated avalanche release

date based on other available Sentinel-1 images. Each RGB-composite can have one or more estimated avalanche release dates. This enables an opportunity for differences in greenness within an image. An avalanche occurring subsequent to the reference acquisition date is expected to exhibit greater weathering effects on its surface, compared to an avalanche occurring prior to the activity acquisition date. Thus, greenness values could differ despite being in the same RGB-composite, depending on when the avalanche occurred. The effect on the greenness of detections with different avalanche release dates within the same RGB-composite was not studied extensively. However, we can determine that individual detections in a RGB-composite do contain diverse greenness values despite having equally estimated avalanche release dates (Figure 4.5).

## 6.4 Evaluation of the greenness method

We chose to consider the top 15% of change detection images as many detections in each respective region, related to a coverage of 66.1% and 57.2% of the total detections in the dataset for Lyngen and Romsdal, respectively. This equals a threshold considered as many as 84 detections or more in Lyngen, and 96 or more in Romsdal. For a reference, the maximum number of detections in one RGB-composite is 468 in Lyngen and 269 in Romsdal. The in total 16 change detection images used in our analysis were selected randomly among images with many detections. This led to that images with detections barely above the limit, yielding few detections in the smaller areas used for the analysis. When removing the lower quartile of high influential data points, the affected data points were mostly from the smallest areas with the fewest detections in the RGB-composites. Alternative methods for choosing images with many detections could be considering only the top images with the most detections or the outliers in the histograms in Figure 3.10 and 3.11. This would potentially fix the problem with few detections in some areas. Nevertheless, this is not guaranteed, e.g., due to placement of areas, avalanche terrain or other spatio-temporal factors regarding when and where avalanches occur). On another note, what is meant by many is a matter of definition. With a median of respectively 12 and 19 detections per change detection image in Lyngen and Romsdal, respectively, most of the data has fewer detections. Thus, while a lower threshold may be feasible, it may not significantly contribute to our analysis due to insufficient data, and a higher threshold may prove more advantageous.

The interpretation of true and false images is subject to certain limitations. This process is undertaken manually by an untrained student, albeit with the aid of supervisors. On the other side, all available resources for verifying the accuracy of these assessments have been utilized. The images have been meticulously examined, utilizing weather data and RegObs. An additional contentious issue pertains to determining the threshold for the number of

true detections necessary to confirm the validity of a change detection image. For instance, if an area contains 100 detections, of which 90 are deemed false positives, valuable information may still be contained within the 10 genuine detections.

The choice of creating smaller areas was deemed necessary to facilitate the identification of potentially true and false detections, which can be arduous to discern within extensive images, given the potential for local variations within large areas. The placement of these smaller areas was randomly determined within areas that exhibited numerous visual detections. Initially, we considered utilizing two smaller areas in each region. However, we eventually expanded this to six smaller areas to allow for the reusability of data from selected images. In hindsight, if we had the opportunity to reconsider, we might have preferred fewer areas in each region and instead opted to incorporate additional images as this could provide more insightful results. However, such a choice would be more time-consuming, and our selection of the number of RGB-composites and areas has provided results.

We chose to delineate four distinct zones, namely non-avalanche terrain (NONE), avalanche terrain (AT), detection area (DET), and a buffer zone of 40 meters (B40). Notably, we have not distinguished the detection areas within the avalanche terrain. This approach has both advantages and disadvantages. On the one hand, it enables us to observe a discernible increase from the non-avalanche terrain to the avalanche terrain, as the avalanche terrain contains the detections. Otherwise, NONE and AT are hypothesised to be more similar, as neither zone contains detections. The size of AT is substantial enough to exhibit a noticeable difference from the detection area. Alternatively, the removal of the detections from the avalanche terrain mask could be useful to explore differences in greenness values between the non-avalanche terrain and the avalanche terrain, as the latter often is located in higher altitudes. As seen in the case studies, a transition from wet to dry snow conditions is not necessarily conditioned to all altitudes. This could provide valuable insight into potentially increased backscatter values for higher altitudes. However, the difference between NONE and AT is relatively minimal.

The decision to select a buffer zone of 40 meters is based on our aim to have an area comparable to the detection zone in terms of size and statistical properties, as well as divisible by 20 meters to match the pixel resolution of 20 x 20 meters. Initially, we explored by using a buffer zone of 60 meters, and also a buffer zone of 120 meters was considered. It may be worth exploring how our results change by using a larger buffer zone, as this would encompass a greater area of the terrain around the detection polygon.

# CHAPTER 7

# Conclusion

SatSkred allows for the automatic detection of avalanche debris. By utilizing the temporal backscatter change between two Sentinel-1 SAR images, avalanche deposits are detectable due to the increased surface roughness leading to a high relative backscatter. The transition from wet to dry snow conditions is known to produce many false detections, resulting from a relative increase in backscatter.

We have successfully developed a greenness indicator as a proxy for increased backscatter values that quantifies the band values in a change detection image (RGB-composite). The RGB-composite is composed of two S1 images with similar geometry and track, originating from a 6- or 12-day cycle. The greenness indicator provides each pixel in the RGB-composite with a value between -1 (maximum decrease) and 1 (maximum increase), explaining the relative backscatter change in each individual pixel. Following, a zonal greenness analysis was conducted on scenarios in the dataset with high avalanche activity. The greenness indicator was used to calculate the mean greenness in four zones: non-avalanche terrain, avalanche terrain, detection area and a 40-meter buffer zone surrounding each detection polygon. The mean greenness values were further analysed to discern whether the greenness indicator could contribute to filtering false detections from true detections.

The findings of our study demonstrate a correlation between the greenness values in the non-avalanche terrain and the avalanche terrain, as well as between the detection area and the buffer zone. Further, our results indicate that a greenness contrast of minimum 0.25 between the buffer zone and detection area, and 0.48 between the avalanche terrain and detection area, effectively eliminate numerous false detections in our dataset. Moreover, a case study was conducted on previously unanalysed RGB-composites to test our threshold values. The snow conditions defined the cases between the two acquisition dates as a wet-to-dry transition (case A) and no transition (case B). The contrast values were analysed in context with meteorological data and the interpretation of RGB-composites.

The results from our case studies suggest that the greenness threshold of 0.48 between the detection area and avalanche terrain is more sensitive to accept falsely detected avalanche deposits in RGB-composites influenced by a high increase in relative backscatter. The greenness threshold of 0.25 between the detection area and the buffer zone is believed to be more successful in classifying the rightful detections as true or false. As evidenced by our zonal greenness analysis and case studies, the threshold excluded 83% of the potentially false detections and included 92% of the potentially true detections. Compared to the contrast threshold between the buffer zone and detection area, 78% of false detections were excluded, and 73% of true detections were included.

Our approach is somewhat successful in filtering potentially false detections from potentially true detections, and is believed to be important in a further development of the automatic change detection algorithm. Still, further testing is considered necessary. One suggestion is to evaluate the threshold values on a large set of previously analysed RGB-composites containing both true and false detections. This could be done similarly to the method for quality-flagging in the original detection algorithm. Additionally, even lower threshold values could be considered, although this would most likely include more false detections.

# Appendices

# Appendix

## Informative tables

This section provides informative tables regarding the attributes used to describe each detection by the SatSkred algorithm, chosen RGB-composites for the greenness analysis and an overview of the number of detections in each area and RGB-composite.

Table 1: Overview of SatSkred attributes used to describe each auto-detected avalanche debris. Description is translated to English.

| **Attribute** | **Description** |
|---|---|
| OBJECTID | Unique number for each feature in dataset |
| skredTidspunkt | Date and time for predicted avalanche release time |
| Dato | Date for predicted avalanche release time |
| Tidsnøyaktighet | Temporal precision in hours or days |
| registrertDato | Date and time for registration of detection |
| registrertAv | Registered by |
| Kvalitet | Acceptance quality |
| objektType | Type of object |
| X | x-coordinate of detection |
| Y | y-coordinate of detection |
| skredID | Unique number for each detection |
| ansvarligInstitusjon | Responsible institution |
| eksposisjonUtlopsomr | Cardinal direction |
| snittHelningUtlopssomr | Mean slope for detection |
| maksHelningUtlopsomr | Maximum slope for detection |
| minHelningUtlopsomr | Minimum slope for detection |
| Høyde | Height |
| noyHoydeStoppSkred | Height of debris |
| baneFlagg | Flag for lane |
| veiFlagg | Flag for road |
| elvenettFlagg | Flag for river |
| bebyggelseProsent | Percentage developed areas |
| jordbrukProsent | Precentage agriculture |
| breProsent | Precentage glacier |
| kjenteSkredlopProsent | Percentage known avalanche paths |
| regions_id | Four-digits region ID |
| Varslingsregion | Name of forecast region |
| safeName | Name of forecast region |
| SHAPE_Length | Length of detection |
| SHAPE_Area | Area of detection |

Table 2: Overview of the selected images for the Zonal Greenness Analysis. Image names include time stamp for activity image (T1), reference image (T0) and track number. The total number of detections (tot_det) made in the NAWS region and number of detections covered by the smaller areas (area_det) are shown as a coverage percentage.

| Image name [T1, T0, track] | Region | tot_det | area_det | Coverage[%] |
|---|---|---|---|---|
| rgb_t1_20190409T161447_t0_20190403T161514_track_131_copol_VV | Lyngen | 266 | 134 | 50.36 |
| rgb_t1_20190504T160704_t0_20190422T160703_track_058_copol_VV | Lyngen | 468 | 3 15 | 67.31 |
| rgb_t1_20191209T051158_t0_20191203T051112_track_095_copol_VV | Lyngen | 318 | 221 | 69.5 |
| rgb_t1_20191211T161522_t0_20191205T161437_track_131_copol_VV | Lyngen | 120 | 86 | 71.67 |
| rgb_t1_20200104T161521_t0_20191229T161436_track_131_copol_VV | Lyngen | 247 | 157 | 63.56 |
| rgb_t1_20200331T052030_t0_20200325T051921_track_168_copol_VV | Lyngen | 187 | 110 | 58.82 |
| rgb_t1_20201109T051205_t0_20201103T051119_track_095_copol_VV | Lyngen | 132 | 106 | 80.30 |
| rgb_t1_20210217T155915_t0_20210211T155819_track_160_copol_VV | Lyngen | 455 | 345 | 75.82 |
| rgb_t1_20190402T171106_t0_20190327T171046_track_117_copol_VV | Romsdal | 196 | 93 | 47.45 |
| rgb_t1_20190503T170313_t0_20190421T170312_track_044_copol_VV | Romsdal | 150 | 93 | 62.00 |
| rgb_t1_20200110T054656_t0_20200104T054631_track_037_copol_VV | Romsdal | 96 | 66 | 68.75 |
| rgb_t1_20200214T171052_t0_20200208T171109_track_117_copol_VV | Romsdal | 142 | 113 | 79.58 |
| rgb_t1_20200403T170318_t0_20200328T170234_track_044_copol_VV | Romsdal | 129 | 69 | 53.49 |
| rgb_t1_20200503T170236_t0_20200427T170319_track_044_copol_VV | Romsdal | 103 | 60 | 58.25 |
| rgb_t1_20200514T171125_t0_20200508T171054_track_117_copol_VV | Romsdal | 269 | 128 | 47.58 |
| rgb_t1_20200527T170237_t0_20200521T170320_track_044_copol_VV | Romsdal | 246 | 104 | 42.28 |

Table 3: Distribution of detections per image and area. Header refers to T1 timestamp in Table A2. For full details of time (HH:MM:SS) for acquisition date see Table A2. AM and PM are used as a reference to time to save space.

| Area | 091219AM | 090419PM | 040519PM | 040120PM | 091120AM | 170221PM | 310320AM | 111219PM | Tot |
|---|---|---|---|---|---|---|---|---|---|
| L1 | 80 | 49 | 81 | 50 | 41 | 90 | 24 | 16 | 431 |
| L2 | 13 | 23 | 36 | 16 | 5 | 53 | 21 | 19 | 186 |
| L3 | 60 | 21 | 45 | 33 | 9 | 40 | 21 | 8 | 237 |
| L4 | 26 | 17 | 59 | 21 | 18 | 73 | 21 | 12 | 247 |
| L5 | 23 | 16 | 45 | 22 | 11 | 57 | 17 | 21 | 212 |
| L6 | 19 | 8 | 49 | 15 | 22 | 32 | 6 | 10 | 161 |
| Total | 221 | 134 | 315 | 157 | 106 | 345 | 110 | 86 | 1471 |

| Area | 020419PM | 030519PM | 140520PM | 030420PM | 100120AM | 270520PM | 140220PM | 030520PM | Tot |
|---|---|---|---|---|---|---|---|---|---|
| R1 | 23 | 28 | 23 | 21 | 6 | 17 | 24 | 0 | 142 |
| R2 | 6 | 5 | 19 | 7 | 6 | 8 | 2 | 15 | 68 |
| R3 | 21 | 16 | 31 | 10 | 28 | 18 | 18 | 14 | 156 |
| R4 | 40 | 30 | 43 | 27 | 25 | 28 | 52 | 14 | 259 |
| R5 | 0 | 12 | 6 | 0 | 1 | 25 | 3 | 15 | 62 |
| R6 | 3 | 2 | 6 | 4 | 0 | 8 | 14 | 2 | 39 |
| Total | 93 | 93 | 128 | 69 | 66 | 104 | 113 | 60 | 726 |

## Buffer zone

We wanted our buffer zone to be of similar size and statistics as the zone containing detections. Statistics of the area to buffer zones with widths of 20, 40, 60 and 120 meters were compared against the the area of detections of a total of 2659 individual detections, originating from four RGB-composites in each region (Figure 1, Table 4). The width of 40 meters was chosen based on the most similar average, in combination with a higher maximum area. A width of 20 meters would have been more similar to the median area, but we would have missed larger areas.

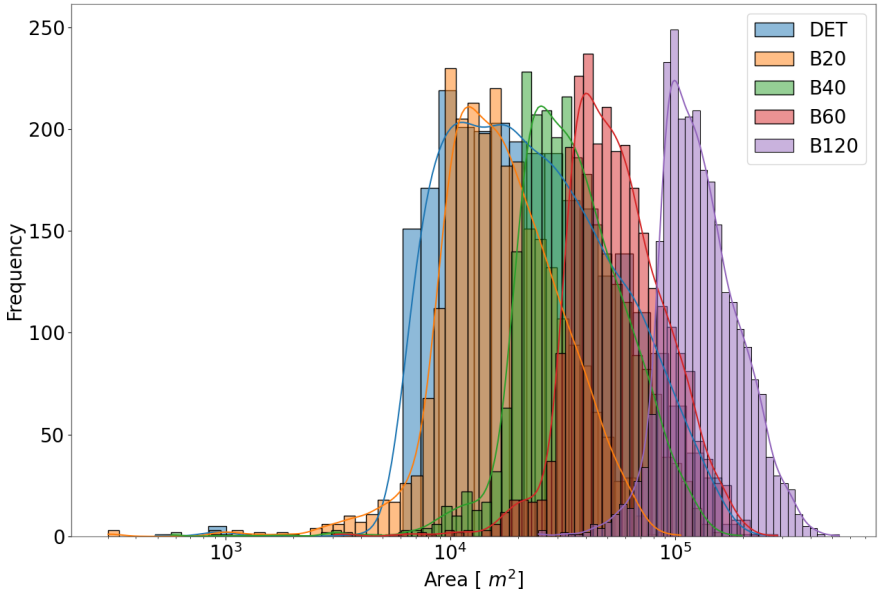


Figure 1: Histogram showing distribution of different widths on buffer zones compared to detections. B20 = 20 meters buffer, etc.

Table 4: Statistics of different widths on buffer zones. All values are in $m^2$.

| | DET | B20 | B40 | B60 | B120 |
|---|---|---|---|---|---|
| count | 2659.00 | 2659.00 | 2659.00 | 2659.00 | 2659.00 |
| mean | 32481.61 | 20037.59 | 40144.38 | 61937.78 | 140072.38 |
| std | 29795.44 | 12524.60 | 22728.71 | 32211.73 | 59247.22 |
| min | 488.00 | 301.00 | 574.00 | 3035.00 | 24662.00 |
| 25% | 11765.50 | 11262.75 | 24167.50 | 39229.00 | 97839.00 |
| 50% | 21310.00 | 16291.50 | 33399.00 | 52660.00 | 123682.00 |
| 75% | 42458.00 | 25089.25 | 49727.50 | 75667.50 | 166530.00 |
| max | 275985.00 | 105700.00 | 197634.00 | 284848.00 | 535668.00 |

### Dataset from zonal greenness analysis

This section provides an overview of the dataset resulting from the zonal greenness analysis. The table containing potentially true data points is seen in Table 5, while the table containing potentially false data points is seen in Table 6. Statistics from the analysis dataset containing the high-influential data points are seen in Table 7.

Table 5: Zonal greenness results from analysis over potentially true detections. Data points considered as HIDP are not included.

| T1 | Area | NONE | AT | DET | B40 |
|---|---|---|---|---|---|
| 02.04.2019 17:11 | R1 | 0.0455 | 0.0056 | 0.6995 | 0.1970 |
| 02.04.2019 17:11 | R3 | -0.1274 | -0.0744 | 0.5874 | 0.0895 |
| 02.04.2019 17:11 | R4 | -0.2024 | -0.1030 | 0.7058 | 0.1394 |
| 04.05.2019 16:07 | L1 | -0.0625 | -0.0318 | 0.7696 | 0.3838 |
| 04.05.2019 16:07 | L2 | -0.0492 | 0.0427 | 0.6328 | 0.2932 |
| 04.05.2019 16:07 | L3 | 0.0062 | 0.0242 | 0.6328 | 0.2932 |
| 04.05.2019 16:07 | L4 | 0.0363 | 0.0968 | 0.6953 | 0.4131 |
| 04.05.2019 16:07 | L5 | -0.0812 | 0.0445 | 0.6617 | 0.3723 |
| 04.05.2019 16:07 | L6 | -0.1181 | 0.0316 | 0.6196 | 0.2933 |
| 09.12.2019 05:11 | L1 | 0.0241 | -0.0264 | 0.4336 | 0.0735 |
| 09.12.2019 05:11 | L2 | 0.0532 | -0.0175 | 0.3011 | 0.0404 |
| 09.12.2019 05:11 | L3 | 0.0050 | -0.0029 | 0.4297 | 0.1088 |
| 09.12.2019 05:11 | L4 | 0.0045 | 0.0102 | 0.2779 | 0.0994 |
| 09.12.2019 05:11 | L5 | 0.0116 | 0.0104 | 0.2736 | 0.0739 |
| 09.12.2019 05:11 | L6 | 0.0007 | -0.0073 | 0.3827 | 0.0994 |
| 10.01.2020 05:46 | R3 | 0.0278 | 0.0123 | 0.4279 | 0.1298 |
| 10.01.2020 05:46 | R4 | 0.0787 | 0.0836 | 0.6426 | 0.2634 |
| 03.04.2020 17:03 | R1 | 0.0706 | 0.0893 | 0.7587 | 0.4751 |
| 03.04.2020 17:03 | R3 | 0.0792 | 0.1000 | 0.7503 | 0.4752 |
| 03.04.2020 17:03 | R4 | 0.1724 | 0.1518 | 0.7040 | 0.4391 |
| 14.05.2020 17:11 | R1 | -0.2810 | -0.1557 | 0.7883 | 0.3654 |
| 14.05.2020 17:11 | R2 | 0.1744 | 0.1232 | 0.7315 | 0.3197 |
| 14.05.2020 17:11 | R3 | 0.0007 | -0.0110 | 0.7135 | 0.3197 |
| 14.05.2020 17:11 | R4 | 0.0053 | 0.0048 | 0.8601 | 0.4092 |
| 27.05.2020 17:02 | R3 | -0.2649 | 0.1127 | 0.6126 | 0.1913 |
| 27.05.2020 17:02 | R4 | -0.4095 | -0.0896 | 0.5404 | 0.2404 |

Table 6: Zonal greenness results from analysis over potentially false detections. Data points considered as HIDP are not included.

| T1 | Area | NONE | AT | DET | B40 |
|---|---|---|---|---|---|
| 09.04.2019 16:14 | L1 | 0.0150 | 0.0368 | 0.5754 | 0.3036 |
| 09.04.2019 16:14 | L2 | 0.1708 | 0.0916 | 0.5506 | 0.4298 |
| 09.04.2019 16:14 | L3 | 0.0505 | 0.0583 | 0.5757 | 0.3533 |
| 09.04.2019 16:14 | L4 | 0.0533 | 0.0491 | 0.5096 | 0.3202 |
| 09.04.2019 16:14 | L5 | 0.0269 | 0.0393 | 0.5385 | 0.3834 |
| 03.05.2019 17:03 | R1 | 0.0036 | 0.0356 | 0.4171 | 0.2147 |
| 03.05.2019 17:03 | R3 | -0.2268 | -0.1180 | 0.4500 | 0.1090 |
| 03.05.2019 17:03 | R4 | -0.3241 | -0.1386 | 0.4241 | 0.0748 |
| 11.12.2019 16:15 | L1 | 0.3339 | 0.2332 | 0.5833 | 0.3807 |
| 11.12.2019 16:15 | L2 | 0.2598 | 0.2114 | 0.4704 | 0.3276 |
| 11.12.2019 16:15 | L4 | 0.2238 | 0.1429 | 0.4704 | 0.3276 |
| 11.12.2019 16:15 | L5 | 0.2635 | 0.1436 | 0.4377 | 0.2637 |
| 11.12.2019 16:15 | L6 | 0.2378 | 0.2137 | 0.5476 | 0.3383 |
| 04.01.2020 16:15 | L1 | 0.0770 | 0.0614 | 0.5027 | 0.2621 |
| 04.01.2020 16:15 | L2 | 0.0216 | 0.0616 | 0.3576 | 0.2223 |
| 04.01.2020 16:15 | L3 | 0.0086 | 0.0794 | 0.4024 | 0.2253 |
| 04.01.2020 16:15 | L4 | 0.0648 | 0.0549 | 0.4514 | 0.2451 |
| 04.01.2020 16:15 | L5 | 0.0794 | 0.0553 | 0.4957 | 0.3276 |
| 04.01.2020 16:15 | L6 | 0.0190 | 0.0471 | 0.5140 | 0.2915 |
| 14.02.2020 17:10 | R1 | 0.0941 | 0.0927 | 0.5258 | 0.3809 |
| 14.02.2020 17:10 | R3 | 0.0093 | -0.0115 | 0.3486 | 0.0712 |
| 14.02.2020 17:10 | R4 | 0.0815 | 0.0880 | 0.4230 | 0.2183 |
| 31.03.2020 05:20 | L1 | 0.0289 | 0.0594 | 0.4577 | 0.2651 |
| 31.03.2020 05:20 | L2 | 0.0424 | 0.0846 | 0.5550 | 0.3373 |
| 31.03.2020 05:20 | L3 | -0.0615 | 0.0848 | 0.4736 | 0.3073 |
| 31.03.2020 05:20 | L4 | 0.0891 | 0.0784 | 0.5002 | 0.2865 |
| 31.03.2020 05:20 | L5 | 0.0353 | 0.0675 | 0.4509 | 0.3103 |
| 31.03.2020 05:20 | L6 | 0.0502 | 0.0749 | 0.7029 | 0.3577 |
| 03.05.2020 17:02 | R2 | -0.1325 | -0.1457 | 0.5252 | 0.3022 |
| 03.05.2020 17:02 | R3 | -0.0926 | -0.0837 | 0.5491 | 0.1894 |
| 09.11.2020 05:12 | L1 | -0.0226 | -0.1086 | 0.4251 | 0.1667 |
| 09.11.2020 05:12 | L3 | -0.0214 | -0.0727 | 0.3592 | 0.1596 |
| 09.11.2020 05:12 | L4 | -0.0368 | 0.0009 | 0.3406 | 0.1543 |
| 09.11.2020 05:12 | L5 | -0.0335 | 0.0154 | 0.4350 | 0.2064 |
| 09.11.2020 05:12 | L6 | -0.0627 | -0.0722 | 0.3788 | 0.1970 |
| 17.02.2021 15:51 | L1 | 0.0156 | 0.0638 | 0.3673 | 0.1289 |
| 17.02.2021 15:51 | L2 | -0.1009 | 0.0721 | 0.3516 | 0.1292 |
| 17.02.2021 15:51 | L3 | 0.0308 | 0.0548 | 0.2800 | 0.1272 |
| 17.02.2021 15:51 | L4 | 0.0274 | 0.0632 | 0.2851 | 0.1040 |
| 17.02.2021 15:51 | L5 | 0.0299 | 0.0737 | 0.2790 | 0.1215 |
| 17.02.2021 15:51 | L6 | 0.0366 | 0.0677 | 0.2390 | 0.1141 |

Table 7: Statistics from the zonal greenness analysis with N=90 observations. The table includes statistics on the count, the sum and the mean greenness in the four distinct zones. High influential data points (<25%) were removed, equal to a cutoff threshold of 751.5 pixels in DET pixel count.

| | **NONE** | | | **AT** | | |
|---|---|---|---|---|---|---|
| | count | sum | GI | count | sum | GI |
| no. obs | 90 | 90 | 90 | 90 | 90 | 90 |
| mean | 97820.66 | -966.60 | -0.0015 | 277656.24 | 7097.80 | 0.0206 |
| std | 68448.55 | 20553.10 | 0.1609 | 123405.53 | 27281.00 | 0.1047 |
| min | 33115.00 | -90247.41 | -0.4181 | 72265.30 | -56919.70 | -0.2582 |
| 25% | 41685.75 | -3460.66 | -0.0622 | 194709.78 | -5432.24 | -0.0257 |
| 50% | 83137.00 | 1227.65 | 0.0175 | 260951.87 | 8689.72 | 0.0380 |
| 75% | 111530.25 | 5340.63 | 0.0678 | 372066.45 | 22049.74 | 0.0791 |
| max | 256975.00 | 72966.63 | 0.5043 | 543593.85 | 118900.23 | 0.3265 |

| | **DET** | | | **B40** | | |
|---|---|---|---|---|---|---|
| | count | sum | GI | count | sum | GI |
| no. obs | 90 | 90 | 90 | 90 | 90 | 90 |
| mean | 1882.39 | 962.98 | 0.5026 | 2342.39 | 541.97 | 0.2285 |
| std | 1429.83 | 835.75 | 0.1521 | 1832.04 | 467.85 | 0.1846 |
| min | 33.00 | 30.49 | 0.1835 | 40.00 | -158.32 | -0.7196 |
| 25% | 751.50 | 376.68 | 0.4029 | 1084.00 | 192.69 | 0.1293 |
| 50% | 1641.00 | 781.41 | 0.4976 | 1973.00 | 479.42 | 0.2488 |
| 75% | 2549.00 | 1339.94 | 0.5864 | 3160.00 | 795.56 | 0.3309 |
| max | 6429.00 | 4673.68 | 0.9237 | 8549.00 | 2311.40 | 0.7176 |

# List of Figures

# List of Tables

# Bibliography


Antonova, S., Kääb, A., Heim, B., Langer, M. and Boike, J. (2016). 'Spatio-temporal variability of X-band radar backscatter and coherence over the Lena River Delta, Siberia'. In: *Remote sensing of Environment* vol. 182, pp. 169–191.

Attema, E., Bertoni, R., Bibby, D., Carbone, A., Cosimo, G. d., Geudtner, D., Giulicchi, L., Lokas, S., Navas-traver, I., Ostergaard, A. et al. (2012). 'Sentinel-1: ESA's Radar Observatory Mission for GMES Operational Services'. In: *ESA SP-1322/1*. ESA Communications.

Baumgartner, F., Jezek, K., Forster, R., Gogineni, S. and Zabel, I. (1999). 'Spectral and angular ground-based radar backscatter measurements of Greenland snow facies'. In: *IEEE 1999 International Geoscience and Remote Sensing Symposium. IGARSS'99 (Cat. No. 99CH36293)*. Vol. 2. IEEE, pp. 1053–1055.

Eckerstorfer, M., Bühler, Y., Frauenfelder, R. and Malnes, E. (2016). 'Remote sensing of snow avalanches: Recent advances, potential, and limitations'. In: *Cold Regions Science and Technology* vol. 121, pp. 126–140.

Eckerstorfer, M. and Malnes, E. (2015). 'Manual detection of snow avalanche debris using high-resolution Radarsat-2 SAR images'. In: *Cold Regions Science and Technology* vol. 120, pp. 205–218.

Eckerstorfer, M., Malnes, E. and Müller, K. (2017). 'A complete snow avalanche activity record from a Norwegian forecasting region using Sentinel-1 satellite-radar data'. In: *Cold regions science and technology* vol. 144, pp. 39–51.

Eckerstorfer, M., Malnes, E. and Vickers, H. (2018). *Worldwide avalanche detection using Sentinel-1: Service prospectus*. Tech. rep. Norut.

Eckerstorfer, M., Oterhals, H. D., Müller, K., Malnes, E., Grahn, J., Langeland, S. and Velsand, P. (2022). 'Performance of manual and automatic detection of dry snow avalanches in Sentinel-1 SAR images'. In: *Cold Regions Science and Technology* vol. 198, p. 103549.

Eckerstorfer, M., Vickers, H., Malnes, E. and Grahn, J. (2019). 'Near-real time automatic snow avalanche activity monitoring system using Sentinel-1 SAR data in Norway'. In: *Remote Sensing* vol. 11, no. 23, p. 2863.

ESA (2023a). *End of mission of the Copernicus Sentinel-1B Satellite*. Accessed: 2023-05-04. URL: https://sentinels.copernicus.eu/web/sentinel/-/end-of-mission-of-the-copernicus-sentinel-1b-satellite/1.5.

— (2023b). *Sentinel-1: Mission summary*. Accessed: 2023-01-15. URL: https://sentinels.copernicus.eu/web/sentinel/missions/sentinel-1/overview/mission-summary.

— (2023c). *Sentinel-1: SAR instrument*. Accessed: 2023-01-15. URL: https://sentinel.esa.int/web/sentinel/technical-guides/sentinel-1-sar/sar-instrument.

Fierz, C., Armstrong, R., Durand, Y., Etchevers, P., Greene, E., McClung, D., Nishimura, K., Satyawali, P. and Sokratov, S. (2009). *The International Classification for Seasonal Snow on the Ground*. IHP-VII Technical Documents in Hydrology No83, IACS Contribution No1, UNESCO-IHP, Paris.

Lied, K. and Kristensen, K. (2003). *Snøskred: håndbok om snøskred*. Vett & Viten.

Lillesand, T., Kiefer, R. W. and Chipman, J. (2015). *Remote sensing and image interpretation*. John Wiley & Sons.

Malnes, E., Eckerstorfer, M. and Vickers, H. (2015). 'First Sentinel-1 detections of avalanche debris'. In: *The Cryosphere Discussions* vol. 9, no. 2, pp. 1943–1963.

Malnes, E., Eckerstorfer, M., Larsen, Y., Frauenfelder, R., Jonsson, A., Jaedicke, C. and Solbø, S. A. (2013). 'Remote sensing of avalanches in northern Norway using Synthetic Aperture Radar'. In: *Proceedings of the International Snow Science Workshop*, pp. 955–959.

Martinez-Vazquez, A. and Fortuny-Guasch, J. (2006). 'Feasibility of snow avalanche volume retrieval by GB-SAR imagery'. In: *2006 IEEE International Symposium on Geoscience and Remote Sensing*. IEEE, pp. 743–746.

— (2008). 'A GB-SAR processor for snow avalanche identification'. In: *IEEE Transactions on Geoscience and Remote Sensing* vol. 46, no. 11, pp. 3948–3956.

McClung, D. and Schaerer, P. A. (2006). *The avalanche handbook*. The Mountaineers Books.

McClung, D. (2002). 'The elements of applied avalanche forecasting, Part I: The human issues'. In: *Natural Hazards* vol. 26, pp. 111–129.

Moreira, A., Prats-Iraola, P., Younis, M., Krieger, G., Hajnsek, I. and Papathanassiou, K. P. (2013). 'A tutorial on synthetic aperture radar'. In: *IEEE Geoscience and remote sensing magazine* vol. 1, no. 1, pp. 6–43.

Müller, K., Kosberg, S., Barfod, E., Rustad, B. K. and Landrø, M. (2013). 'Snøskredvarslingen'. In: URL: https://nve.brage.unit.no/nve-xmlui/bitstream/handle/11250/2497310/rapport2013_65.pdf?sequence=1&isAllowed=y.

Schweizer, J., Bartelt, P. and Herwijnen, A. van (2015). 'Snow Avalanches'. In: *Snow and ice-related hazards, risks, and disasters*. Elsevier, pp. 395–428.

Schweizer, J., Jamieson, J. B. and Schneebeli, M. (2003). 'Snow avalanche formation'. In: *Reviews of Geophysics* vol. 41, no. 4.

Statham, G., Haegeli, P., Greene, E., Birkeland, K., Israelson, C., Tremper, B., Stethem, C., McMahon, B., White, B. and Kelly, J. (2018). 'A conceptual model of avalanche hazard'. In: *Natural Hazards* vol. 90, pp. 663–691.

Torres, R., Snoeij, P., Geudtner, D., Bibby, D., Davidson, M., Attema, E., Potin, P., Rommen, B., Floury, N., Brown, M. et al. (2012). 'GMES Sentinel-1 mission'. In: *Remote sensing of environment* vol. 120, pp. 9–24.

Ulaby, F. T., Moore, R. K. and Fung, A. K. (1986). 'Microwave remote sensing: Active and passive. Volume 3-From theory to applications'. In: pp. 1065–2162.

Varsom (2023). Accessed: 2023-05-12. URL: https://www.varsom.no/snoskred/snoskredulykker/snoskredulykker-i-tabell/.

Vickers, H., Eckerstorfer, M., Malnes, E., Larsen, Y. and Hindberg, H. (2016). 'A method for automated snow avalanche debris detection through use of synthetic aperture radar (SAR) imaging'. In: *Earth and Space Science* vol. 3, no. 11, pp. 446–462.

Vickers, H., Eckerstorfer, M., Malnes, E. and Doulgeris, A. (2017). 'Synthetic aperture radar (SAR) monitoring of avalanche activity: An automated detection scheme'. In: *Image Analysis: 20th Scandinavian Conference, SCIA 2017, Tromsø, Norway, June 12–14, 2017, Proceedings, Part II 20*. Springer, pp. 136–146.

Weydahl, D. J. and Eldhuset, K. (2011). 'Høyoppløsnings SAR satellittbilder tatt over fjellpartier ved Bjerkvik i Nord-Norge'. In.

Wiesmann, A., Wegmuller, U., Honikel, M., Strozzi, T. and Werner, C. L. (2001). 'Potential and methodology of satellite based SAR for hazard mapping'. In: *IGARSS 2001. Scanning the Present and Resolving the Future. Proceedings. IEEE 2001 International Geoscience and Remote Sensing Symposium (Cat. No. 01CH37217)*. Vol. 7. IEEE, pp. 3262–3264.